Universität Bremen

ALFRED-WEGENER-INSTITUT
HELMHOLTZ-ZENTRUM FÜR POLAR-
UND MEERESFORSCHUNG

Dissolution of CaCO$_3$ in the present and glacial ocean: A comparison of the effects of different dissolution parameterizations

Author

Dilruba Peya

Matriculation Number: 2992079

Date of Birth: October 26, 1989

Examiner

Prof. Dr. Gerrit Lohmann

Dr. Christoph Völker

MASTERS THESIS

SUBMITTED IN PARTIAL FULFILMENT OF THE REQUIREMENTS FOR THE DEGREE OF

MASTER OF SCIENCE IN ENVIRONMENTAL PHYSICS

Supervised by

Dr. Christoph Völker

Institute of Environmental Physics (IUP)

University of Bremen, Bremen, Germany

October 27, 2017

pep

Declaration

I, Dilruba Peya, herewith declare that I did the written work on my own and only with the means as indicated.

_____

Date   Signature

Abstract

The production of the calcium carbonate minerals calcite and aragonite in the ocean is primarily done by different pelagic calcifying organisms: coccolithophorids, foraminifera and pteropods. The contribution of corals to the production of $CACO_3$ is comparatively small. The surface ocean is supersaturated with respect to the two minerals forms of $CACO_3$: aragonite and calcite, while the deep ocean is undersaturated. Most of these calcium carbonate minerals produced near the surface ocean sink through the water column and mainly dissolve in the deep ocean below the saturation horizon where the solubility product of the minerals increases due to increased pressure. $CaCO_3$ formation in the surface ocean and dissolution in the deeper ocean both affect dissolved inorganic carbon and total alkalinity and also the oceanic pCO$_2$. In this study, a global biogeochemical model (REcoM) is used to analyze the production and dissolution of $CaCO_3$ for the Last Glacial Maximum (LGM) and present day with two different set up of dissolution rate: one is that the dissolution rate of $CaCO_3$ is assumed constant when it sinks through the water column (λ does not depend on Ω), in other λ has been made depend on Ω. In REcoM, biogenic $CaCO_3$ production is restricted to phytoplankton. In comparison with observation, model simulation with uniform dissolution does a good job at reproducing the global patterns of DIC, alkalinity and Ω although some regional differences remain: too high DIC concentrations in between 800 m to 1200 m ocean depth, high alkalinity concentration in the depth between 1200 m to 2000 m and higher Ω in the Atlantic Ocean and the Indian Ocean value. In this study, it is tested that whether changes in the parameterization of the $CaCO_3$ dissolution rate in the model can improve the distribution. Making the dissolution depend on Ω leads to a much improved global oceanic distribution of DIC, alkalinity and Ω. Furthermore, LGM model simulation reproduce the ocean of low temperature, salty and high in alkalinitry and DIC concentration than the present day [Buchanan et al., 2016b, Völker and Köhler, 2013, Zhang et al., 2013]. The overall LGM ocean is high in calcium carbonate saturation than the present day because of higher [CO$_3^{2-}$] concentration.

Acknowledgment

Contents

List of Figures

Abbreviations

AABW	Antarctic Bottom Water
AMOC	Atlantic Meridional Overturning Circulation
CCD	Calcite Compensation Depth
CORE	Common Ocean-Ice Reference Experiment
DIC	Dissolved Inorganic Carbon
DIN	Dissolved Inorganic Nitrogen
DOC	Dissolved Organic Carbon
DOE	Department Of Environment
DON	Dissolved Organic Nitrogen
GNAIW	Glacial North Atlantic Intermediate Water
GLODAP	Global Ocean Data Analysis Project
LGM	Last Glacial Maximum
MITgcm	Massachusetts Institute of Technology general circulation model
NADW	North Atlantic Deep Water
NPIW	North Pacific Intermediate Water
PIC	Particulate Inorganic Carbon
PISCES	Pelagic Interactions Scheme for Carbon and Ecosystem Studies
POC	Particulate Organic Carbon
REcoM	Regulated Ecosystem Model
SST	Sea Surface Temperature
TA	Total Alkalinity
WOA09	World Ocean Atlas 2009

1 Introduction

1.1 Production of CaCO$_3$

The oceanic precipitation of CaCO$_3$ in the open ocean is primarily done biologically by one phytoplanktonic group: coccolithophorids, and two zooplanktonic groups: foraminifera and pteropods. They predominantly occur near the ocean surface but foraminifera also occur at the bottom of the ocean [Sarmiento and Gruber, 2006]. CaCO$_3$ is precipitated usually in the form of calcite and aragonite, two common crystal forms of CaCO$_3$. Coccolithophorids and most foraminifera produce calcite whereas aragonite is produced by pteropods and also by some foraminifera [Zeebe and Wolf-Gladrow, 2001]. Among them, coccolithophores are considered to be the most productive calcifying group [Westbroek et al., 1993] over a large area of the world ocean because of their formation of intensive blooms, especially in subpolar regions [Brown and Yoder, 1994]. Corals are also one of the major calcifying groups in the world ocean and produce a significant amount of calcium carbonate in near-shore environments. About 0.3 Pg C yr^{-1} of CaCO$_3$ is produced by coral reefs mostly in the form of high-magnesium calcite or aragonite, which is roughly a third of the open ocean CaCO$_3$ production [Milliman and Droxler, 1996]. Some part of this CaCO$_3$ could get transported and dissolved into the open ocean. Milliman et al. [1999] state that this transport can be up to 0.1 Pg C yr^{-1}.

By the following calcification equation, it can be seen that the formation of CaCO$_3$ from calcium and bicarbonate ion produces aqueous CO$_2$ which can be used in photosynthesis as source of inorganic carbon [Zondervan et al., 2001]

$$2\text{HCO}_3^- + \text{Ca}^{2+} = \text{CO}_2 + \text{CaCO}_3 + \text{H}_2\text{O} \tag{1}$$
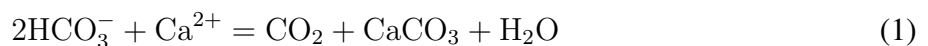
Calcification affects the global and regional carbon budgets by the production of CO$_2$ and CaCO$_3$ and also by fixing of HCO$_3^-$ [Balch et al., 2007]. Recent global estimation of carbonate production is 1.3×10^{14} moles CaCO$_3$ yr^{-1} equivalent to 1.6 Gt Particulate Inorganic Carbon (PIC) yr^{-1} [Balch et al., 2007]. Berelson et al. [2007] estimates the global average carbonate production ranging from 0.5 to 1.6 Gt PIC yr^{-1} whereas the estimated carbonate export (vertical flux of carbonate out of the productive upper layer of the ocean) ranges between 0.4 to 1.8 Gt PIC yr^{-1} based on the analysis of carbonate rain ratio (global average export ratios of CaCO$_3$ to organic carbon) in the water column and on sediment dissolution rates. The difference between production and export can be compared with the oceanic organic carbon cycle. Recently [Jin et al., 2007] summarized global estimates of organic matter export to be 10 to 15 Gt POC yr^{-1} while the global primary production of organic matter varies in the range of 40 to 50 Gt POC

yr^{-1}. The ratio of PIC to particulate organic carbon (POC) is estimated about 0.06 ± 0.03 based on the analysis vertical gradients of potential alkalinity and nitrate [Sarmiento et al., 2002]. Recently Balch et al. [2005] estimate that the ratio between $CaCO_3$ and POC in the euphotic zone is about 0.05 ± 0.01.

1.2 Dissolution of CaCO$_3$

A large fraction of the produced $CaCO_3$ remains intact when the planktonic organisms producing it die or get eaten and subsequently sinks. $CaCO_3$ that is leaving the ocean surface can either be dissolved throughout the water column or at the ocean floor, or get buried [Battaglia et al., 2016]. Dissolution of calcium carbonate is mainly dependent on the saturation state of seawater (Ω) with respect to calcite or aragonite [Sarmiento and Gruber, 2006]. The seawater saturation (Ω) with respect to calcite or aragonite (equation 15) given in chapter 2.1 and can be defined by the product of $[CO_3^{2-}]$ and $[Ca^{2+}]$ ion concentrations divided by the stoichiometric solubility product at the in situ temperature, pressure and salinity [Chung et al., 2003]. The dissolution of $CaCO_3$ minerals is thermodynamically possible when the calcium and carbonate ion concentrations product is below the saturation product in the surrounding environment. Values of omega larger than one ($\Omega > 1$) represent a supersaturated condition of seawater while values of omega smaller than one ($\Omega < 1$) represent undersaturation [Zeebe and Wolf-Gladrow, 2001].

The saturation product of all minerals strongly increases with increasing pressure [Mucci, 1983]. The increase in the pressure with depth leads to increases in solubility of carbonate minerals, causing a decrease of Ω with depth in the ocean. In addition the respiration of organic matter decreases the carbonate ion concentration in the deeper ocean leading to a further decrease in Ω. With respect to the mineral phases of calcium carbonate most of the upper parts of the ocean water column are supersaturated and deep ocean waters are undersaturated [Jansen et al., 2002].

The depth that separates the supersaturated and undersaturated layer is called saturation horizon. This depth is significantly deeper for calcite than aragonite, as aragonite is more soluble than calcite, and also varies from ocean to ocean, being low in high latitudes and the Indian Ocean, high in the Pacific due to the increase of remineralization products with water mass age [Pachauri and Reisinger, 2007].

Figure (1) below shows the difference in saturation horizon of calcite and aragonite in the North Atlantic and North Pacific Ocean. The saturation state of calcite and aragonite is much lower in the North Pacific than in the North Atlantic Ocean. The old ocean waters in the deeper Pacific contain more DIC than in the fresh as Atlantic ocean, due to organic matter remineral-

ization in the deep water. Increased DIC results in a lowering of the carbonate ion concentration in the Pacific Ocean that makes the ocean water more corrosive. This phenomenon is responsible for the difference in lysocline depth both for calcite and aragonite in the North Pacific and North Atlantic Ocean. The lysocline depth is the place in the water column where undersaturation with respect to calcite or aragonite results in a rapid increase in the $CaCO_3$ dissolution rate [Morse, 1974]. With respect to calcite, lysocline depth is about 4000 m (for aragonite, less than 500m) in the Pacific Ocean and about above 4500m (for aragonite, 3000 m) in the Atlantic Ocean [Zeebe and Wolf-Gladrow, 2001].
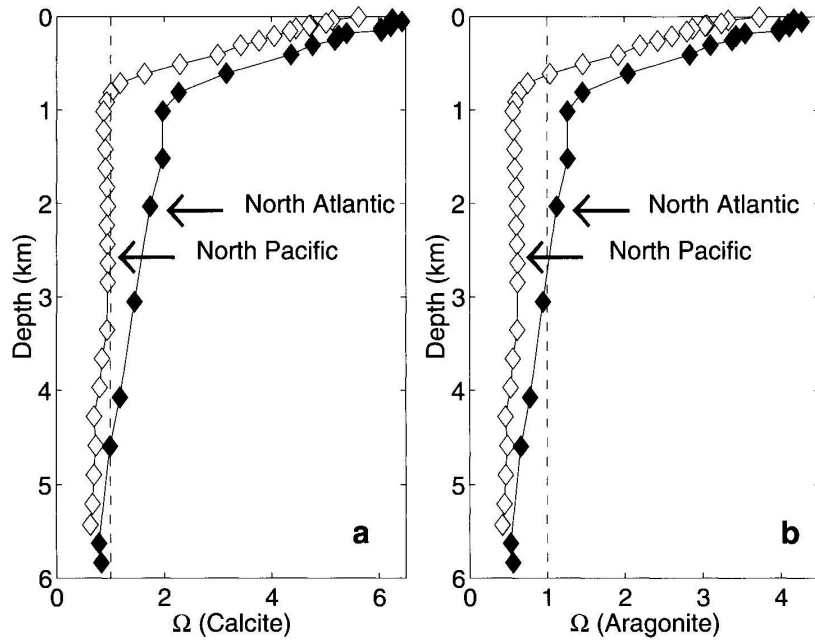
Figure 1: *Schematic diagram of the saturation state of ocean water with respect to calcite and aragonite in the Atlantic and Pacific Ocean as a function of depth. Supersaturation and undersaturation are separated by the vertical dashed line [Zeebe and Wolf-Gladrow, 2001].*

1.2.1 Water column dissolution

This section deals with the water column dissolution of biogenic calcium carbonate minerals while they are sinking through the water column. In general, the dissolution kinetics of calcium carbonate are described by a higher order dependency on the degree of $CaCO_3$ saturation [Gehlen et al., 2007]. For undersaturated water ($\Omega > 1$), one can write the $CaCO_3$ dissolution rate reaction by following [Morse and Berner, 1972].

$$\frac{d[CaCO_3]}{dt} = -[CaCO_3] \cdot k_{CaCO_3}(1 - \Omega)^n \tag{2}$$

3

where k_{CaCO_3} and [CaCO_3] are the dissolution rate and concentration of $CaCO_3$ respectively, and n is the kinetic order of reaction.

In the case of calcite minerals, Keir [1980] proposed a reaction rate order of 4.5 on the basis of laboratory dissolution studies. However, Hales and Emerson [1997a] reevaluated the [Keir, 1980] data and argued that the dissolution rate is linearly dependent on undersaturation (n = 1). Furthermore, first order calcite dissolution kinetics give a better consistency with the interpretation of pH measurements in-situ pore water [Hales and Emerson, 1997a,b]. Recently Arvidson et al. [2003] give an extended reevaluation of carbonate dissolution kinetics and proposed that the reaction is nonlinear, that in most cases the value of n is larger than 1.

The time that sinking particles spend in the water column before arriving at the ocean floor is very short in comparison to the timescale of calcite dissolution in the undersaturated water. That is why it is assumed that the dissolution of carbonate minerals mostly occurs in the sediments [Jansen et al., 2002].

Milliman et al. [1999] calculated however that about 60 – 80 % of the total calcium carbonate dissolution takes place in between 500 and 1000 m depth in the upper ocean, although ocean waters are mostly supersaturated in this depth range with respect to both aragonite and calcite. A possible explanation is that many $CaCO_3$ particles do not sink alone, but together with other particles that contain organic carbon. The respiration of this organic matter can then create a chemical acidic micro-environment around the aggregate, enabling the dissolution in oceanic upper layer supersaturated waters [Jansen et al., 2002].

Jansen et al. [2002] also suggest that water column carbonate dissolution is possible when considering only the calcite, because the sinking rate of individual coccoliths and coccolithophorids is slow, so that it can make possible water column dissolution. The sinking rate of foraminifera and pteropods is so fast that almost no dissolution occurs before reaching the seafloor.

1.2.2 $CaCO_3$ dissolution in the sediment

Sediment dissolution processes play a much more crucial role than water column dissolution for the $CaCO_3$ budget in the world ocean [Sarmiento and Gruber, 2006] as discussed before that the dissolution of $CaCO_3$ mainly occur in deep ocean undersaturated water causing fluxes of Ca^{2+} and alkalinity from sediment. The calcite compensation depth (CCD) is the depth in which the dissolution rate of calcite minerals in sediments is balanced by the supply of the calcite minerals. At this depth, sediments have lost their all calcite minerals due to dissolution [Zeebe and Wolf-Gladrow, 2001]. The CCD strongly varies throughout the world ocean. CCD

gets shallower as Atlantic deep water moves to the Pacific Ocean through the Indian Ocean. The lysocline is generally consistent with the saturation horizon depth and this consistency imply that the variation of the thermodynamic driving factor plays a major role in $CaCO_3$ preservation [Sarmiento and Gruber, 2006].

In the sediment, the dissolution of $CaCO_3$ can also be caused by the process of remineralization. Carbonic acid is produced by organic matter remineralization process within the sediments. Dissolution powered by acid produced in the sediment column is sensitive to the rate of acid production and also to its depth distribution [Boudreau and Canfield, 1993]. The ratio of sinking organic matter (POC) to $CaCO_3$ (PIC) in the deep ocean is on the order of 1:1, [Emerson and Bender, 1981, Archer, 1991] so adequate CO_2 will be available for the dissolution of all $CaCO_3$ in the sediment if all organic carbon material is going through the remineralization process [Sarmiento and Gruber, 2006].

But the permanent burial of a significant portion of the deposited calcium carbonate indicates the variation in relation between organic matter remineralization and $CaCO_3$ dissolution. The reason behind this decoupling is that the remineralization of organic matter occurs very fast in the upper sediment layer while the dissolution kinetics of $CaCO_3$ seems to be slower [Sarmiento and Gruber, 2006]. This difference creates a vertical separation between the very near surface and the deeper layers in the sediments. In consequence, a considerable amount of the free protons from the remineralization in the sediment near surface diffuses out of the sediments and is buffered by the lowermost bottom waters, decreasing the efficiency rate of respiratory-driven dissolution of $CaCO_3$ [Hales, 2003].

1.3 Effects of $CaCO_3$ formation and dissolution on oceanic and atmospheric carbon

CO_2 gas exchange between atmosphere and ocean is regulated by the two marine carbon pumps which are driven by the production of organic matter and calcium carbonate respectively and subsequent sinking to the depth. CO_2 gas exchange depends on the difference between the $p CO_2$ in atmosphere and ocean. The oceanic $p CO_2$ in turn depends on DIC and alkalinity. The organic and $CaCO_3$ pump transport organically bound carbon and $CaCO_3$ from the production site near the surface into the deep ocean, where they slowly get remineralized and dissolved. Both pumps change the DIC and alkalinity at the ocean surface, which affects the $p CO_2$ [Jansen, 2001].

From figure (2) it can be seen that the $p CO_2$ increases with increases of DIC and also with
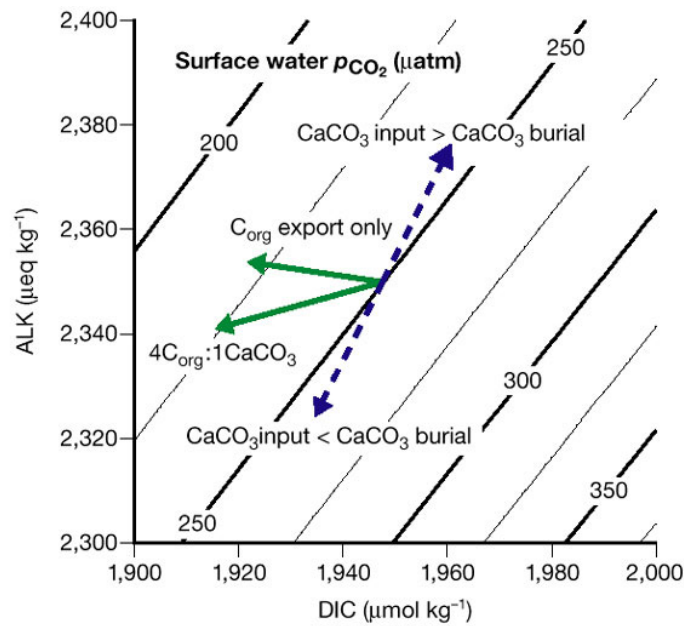
Figure 2: *Formation and dissolution effect of $CaCO_3$ on total alkalinity and dissolved inorganic carbon as well as on oceanic pCO_2 from [Sigman and Boyle, 2000].*

decreases of alkalinity. The resulting effects of an imbalance between $CaCO_3$ production and loss on DIC and alkalinity are shown by the dashed arrows. Oceanic alkalinity and DIC decreases in a 2:1 ratio through the production of $CaCO_3$. A higher input of dissolved calcium carbonate than the burial therefore lowers the pCO_2 of surface waters and increases the oceanic uptake of CO_2 from the atmosphere [Zeebe and Wolf-Gladrow, 2001].

The solid arrows show the effect of the export production (rain of biogenic materials to the deep ocean from the surface). DIC is removed from the surface ocean by export production whereas alkalinity increases in a modest way because of the associated uptake of phytoplanktonic nitrate [Sigman and Boyle, 2000]. Deep ocean DIC and alkalinity are also affected by the export production resulting in a lowering of deep water carbonate ion concentration. This is because, produced surface ocean organic carbon releases DIC by the bacterial microbial oxidation processes in the ocean interior and lowers the deep water carbonate ion concentration [Jansen, 2001]. This processes again affects the burial rate of calcium carbonate in the ocean sediments, which further alters the surface waters pCO_2 through its impact on the total ocean $CaCO_3$ balance (dashed arrows).

2   Model and methods

In this study, a physical and a biogeochemical model is used to simulate the effect of production and dissolution of $CaCO_3$ on the global carbon cycle. As a physical model, the Massachusetts Institute of Technology general circulation model (MITgcm) [Marshall et al., 1997] and as biogeochemical model, the Regulated Ecosystem Model version 2 (REcoM-2) is used. Both the physical and biogeochemical model are described here only in their most important aspects with respect to the carbon cycle. To investigate the glacial-interglacial changes of $CaCO_3$ dissolution, four model simulations have been performed. A summary of these four simulations with their experiment characteristics is shown in table 1.

Name	Boundary conditions	Ω dependency of $CaCO_3$ dissolution	Length of model integration (years)
EXP 01	present-day	Uniform dissolution	1000
EXP 02	present-day	Dissolution depends on Ω	1000
EXP 03	21 ka	Uniform dissolution	3000
EXP 04	21 ka	Dissolution depends on Ω	3000

Table 1: Experimental design of the four different model simulations in this study.

Chapter 3 discusses the baseline experiment EXP 01 and compares the results to a climatology of observations (GLODAP.v2). Results from LGM simulation with uniform dissolution (EXP 03) are discussed in chapter 4 and compared to the EXP 01. Chapter 5 discusses the experiments EXP 02 and EXP 04 in which dissoltion has been made to depend on Ω and compares them to the baseline experiments EXP 01 and EXP 03 for present day and LGM respectively.

2.1   Calculations of the carbonate system in seawater

To analyze both model and observational data, a few calculations of the seawater carbonate chemistry have to be performed. Here therefore I start with a description of these calculations.

Aqueous carbon dioxide (CO_2), bicarbonate HCO_3^- and carbonate ion CO_3^{2-} are the main three forms of carbon dioxide in the Ocean [Zeebe and Wolf-Gladrow, 2001]. The atmosphere - ocean exchange of CO_2 depends on the balance between dissolved CO_2 and atmospheric pCO_2 [figure (3)]. Dissolved CO_2 from atmosphere reacts with seawater. The chemical equilibrium of the carbonate system can be described by the following equation:

$$CO_2 + H_2O \overset{K_1}{\rightleftharpoons} HCO_3^- + H^+ \overset{K_2}{\rightleftharpoons} CO_3^{2-} + 2H^+ \tag{3}$$
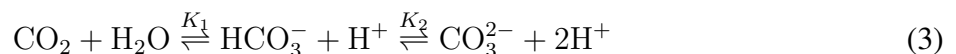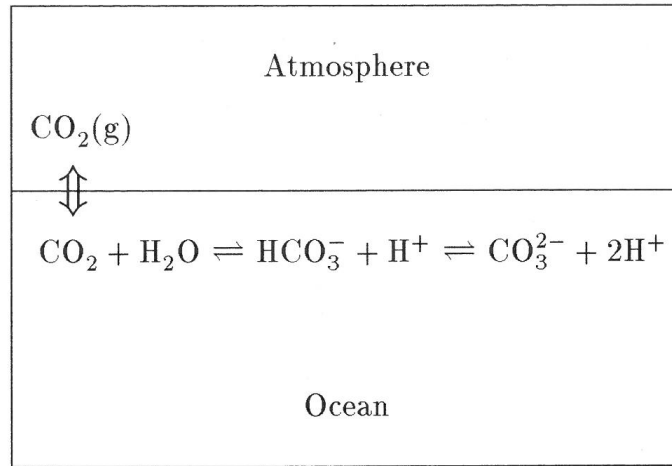
Figure 3: *Schematic diagram of the carbonate system in seawater [p.3 Zeebe and Wolf-Gladrow, 2001, chapter 1].*

K_1 and K_2 are the first and second equilibrium constant of the carbonate system respectively.

Dissolved inorganic carbon (DIC) is defined by sum of the concentrations of the dissolved forms of CO_2, HCO_3, and CO_3^{2-}. In the following, brackets denote the concentration.

$$DIC = [CO_2] + [HCO_3^-] + [CO_3^{2-}] \tag{4}$$

Besides DIC, Alkalinity is another important quantity for the carbonate system that is mainly related to the charge balance in seawater [Zeebe and Wolf-Gladrow, 2001]. Total alkalinity (TA) can be outlined as:

$$TA = [HCO_3^-] + 2[CO_3^{2-}] + [B(OH)_4^-] + [OH^-] - [H^+] + \text{minor species} \tag{5}$$

The minor species further contain small contributions from nutrients that are neglected in this calculation. Carbonate alkalinity (CA) is a part of total alkalinity (TA) and is defined by the following equation:

$$CA = [HCO_3^-] + 2[CO_3^{2-}] \tag{6}$$

In the ocean, the dissolution of calcium carbonate is considered to mainly depend on the saturation state of either calcite or aragonite, the two main crystal forms of $CaCO_3$. The saturation state is primarily determined by the carbonate ion concentration [Zeebe and Wolf-Gladrow, 2001]. The final goal of these calculations is to calculate the saturation state of calcium carbonate in the form of calcite to understand the dissolution of $CaCO_3$ in the world ocean from observational and model data. To do that one has to go through several steps: The first step

would be to calculate the equilibrium stability constants K_1, K_2 for carbonic acid dissociation, and K_b and K_w for boric acid and for water respectively. The equilibrium constants are defined by the following equations:

$$K_1 = \frac{[\text{HCO}_3^-][\text{H}^+]}{[\text{CO}_2]} \tag{7}$$

$$K_2 = \frac{[\text{CO}_3^{2-}][\text{H}^+]}{[\text{HCO}_3^{1-}]} \tag{8}$$

$$K_b = \frac{[\text{B(OH)}_4^-][\text{H}^+]}{[\text{B(OH)}_3]} \tag{9}$$

$$K_w = [\text{H}^+][\text{OH}^-] \tag{10}$$

The constants are given as empirical functions of temperature and salinity. For the equations of equilibrium constants, [Zeebe and Wolf-Gladrow, 2001] have been followed who in turn cite [DOE, 1994].

To calculate the carbonate system, also need to care about Boric acid B(OH)_3 and borate B(OH)_4^- because of their contribution to total alkalinity (TA) [Zeebe and Wolf-Gladrow, 2001]. The total boron concentration B_T

$$B_T = [\text{B(OH)}_4^-] + [\text{B(OH)}_3] \tag{11}$$

mainly depends on seawater salinity and the relation is also given in [Zeebe and Wolf-Gladrow, 2001]. The equilibrium between boric acid and borate is given by

$$\text{B(OH)}_3 + \text{H}_2\text{O} \overset{K_b}{\rightleftharpoons} \text{B(OH)}_4^- + \text{H}^+ \tag{12}$$
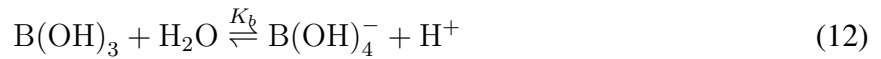
where K_b is the equilibrium constant for boric acid dissociation defined by equation (9)

Pressure has also a small effect on equilibrium constants. Millero [1995] has given a correction for the dependency of the equilibrium constants on pressure. The equation by which one can calculate the effect of pressure on equilibrium constants is also given in [Zeebe and Wolf-Gladrow, 2001]. With the calculated stability constants and DIC, TA specified and B_T, one can calculate the pH. pH is the negative decadal logarithm of H^+ ion concentration. pH can be calculated from DIC and TA by inserting the equilibrium relations from equation (7) and equation (9) into the equation for DIC and TA (equation (4) and equation (5) respectively). This results in two equations for the two unknowns $[\text{CO}_2]$ and $[\text{H}^+]$, which can be combined to one fifth order polynomial for $[\text{H}^+]$ alone. Solving this polynomial will give H^+ ion concentration. With $[\text{H}^+]$ given, one can calculate the carbonate ion concentration as a function of DIC.

$$[\text{CO}_3^{2-}] = \frac{[DIC]K_1K_2}{[\text{H}^+]^2 + [\text{H}^+]K_2 + K_1K_2} \tag{13}$$

Finally, the solubility product of calcite needs to be calculated. The solubility product K_{sp} defines the concentration of $[CO_3^{2-}]$ and $[Ca^{2+}]$ in thermodynamic equilibrium with solid calcite and can be outlined by the following equation [Zeebe and Wolf-Gladrow, 2001].

$$K_{sp} = [Ca_{eq}^{2+}] \cdot [CO_{3_{eq}}^{2-}] \tag{14}$$

Oceanic $[Ca^{2+}]$ variations are quite small and closely related to (proportional) variations in salinity. The relation between salinity and $[Ca^{2+}]$ has been taken from [Zeebe and Wolf-Gladrow, 2001]. So now at the end, one can calculate the saturation state of calcium carbonate (Ω), that is the function of carbonate ion concentration. The $CaCO_3$ saturation state of seawater Ω can be expressed as:

$$\Omega = \frac{[Ca^{2+}][CO_3^{2-}]}{K_{sp}} \tag{15}$$

2.2 The physical model

The MITgcm is a numerical model based on the Navier Stokes equation and the conservation of mass, salt and energy, that has been developed for the study of the large-scale ocean, atmosphere and climate. Because of its possibility for non-hydrostatic modelling, it can be used for small scale process as well [Adcroft et al., 2004]. MITgcm determines the advection and mixing of tracers as a result of the circulation and physical state of ocean i.e. of its velocity, temperature, salinity and pressure fields which are used as prognostic variables in this ocean circulation model [Adcroft et al., 2004]. The setup of the MITgcm model that we use is designed globally at coarse resolution on a grid with $2°$ longitudinal spacing and between $0.38°$ and $2°$ latitudinal spacing. The model domain reaches from $80°$ S to $80°$ N, excluding the Arctic Ocean [Hauck et al., 2013]. For a better resolution of the Southern Ocean, the latitudinal spacing of this model has been made $2°$ times the cosine of latitude. For better resolution of the equatorial current system, resolution around the equator has been increased to about half a degree [Aumont et al., 1999]. The model consists of 30 vertical levels, with layer thickness increasing from 10 m at the surface to 500 m below a depth of 3700 m [Hauck et al., 2013]. The model is forced with an annual climatology of daily wind speed, air temperature, humidity and monthly precipitation and river runoff taken from the CORE data set [Large and Yeager, 2004]. From there forcing fields, heat and freshwater fluxes and wind stress are calculated. For the LGM simulations, monthly averaged atmospheric forcing fields were taken from coupled atmosphere-ocean simulations performed with COSMOS [Zhang et al., 2013] in which boundary conditions and external forcing were imposed according to the PMIP3 protocol for the LGM.

The present day model integration is done over a thousand years. The model is integrated from a state of rest; initial conditions for temperature, salinity, nitrate and silicate were taken from the World Ocean Atlas 2009 (WOA09) [Locarnini et al., 2010, Antonov et al., 2010, Garcia et al., 2010].

The LGM Model run has been integrated over the time of 3000 years. For the LGM runs, sea level has been lowered by 116 m to account for the storage of water in land ice. Total salinity has been made to be conserved, which lead therefore to an increase in ocean salinity by a constant value of around 1 psu. Temperature has been initialized with present-day values, leaving it to the model to equilibrate temperature with the given glacial atmospheric forcing.

The total inventory of tracers (alkalinity, DIC, silicate and phosphate) has been conserved between the present day and LGM runs, i.e. the average concentration has been increased to compensate for the lower ocean volume during the LGM. The partial pressure of atmospheric carbon dioxide pCO_2^{atm} has been set to a fixed pre-industrial value of 280 ppm to a glacial value of 180 ppm for the LGM [Völker and Köhler, 2013].

2.3 The biogeochemical model

The Regulated Ecosystem Model, version 2 (REcoM-2) is used as biogeochemical model in this study. REcoM is based on the [Geider et al., 1998] model in which the internal stoichiometry of phytoplankton cells varies with environmental conditions like light, temperature and nutrient supply. As a result the biochemical composition i.e. the ratio of carbon to chlorophyll (C: Chl) and the ratio of carbon to nitrogen (C: N) in pytoplankton also change with various growth conditions [Geider et al., 1998].

An overall summary of the REcoM-2 model is illustrated in figure (4). In total the REcoM-2
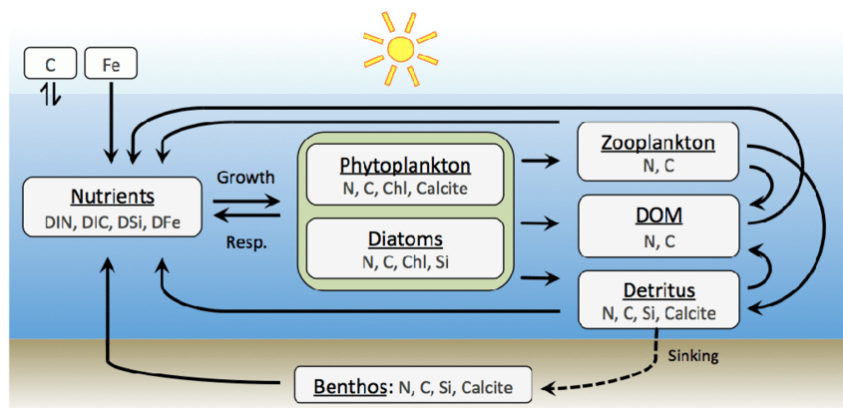

Figure 4: *Schematic diagram of the biogeochemical REcoM-2 model compartments, [Schourup-Kristensen et al., 2014]*

model contains 21 tracers and is divided into different compartments. From figure (4) one can see that the model contains two different functional types of phytoplankton, i.e. nanophytoplankton and diatoms which contain carbon, nitrogen and chlorophyll. Only the nanophytoplankton contains $CaCO_3$ and only the diatoms contain silica. The production of calcium carbonate is described as a function of the gross production of nanophytoplankton [Hauck et al., 2013]. The model also consists of one zooplankton and detritus compartment with organic forms of the main nutrients [Hauck et al., 2013]. The zooplankton compartment consists of nitrogen and carbon pool. Phytoplankton cells are grazed by zooplankton which produce detritus. The zooplanktonic nitrogen and carbon pool can be increased by phytoplankton grazing and decreased by the process of excretion of dissolved organic carbon (DOC) [Hauck et al., 2013]. The heterotrophic carbon pool is the imbalance between uptake of carbon by grazing and loosing by mortality [Hauck et al., 2013]. Detritus compartment contains organic carbon, nitrogen, biogenic silica, iron and calcium carbonate. The detritus sinking speed increases with depth [Kriest and Oschlies, 2008]. The model also contains another compartment with dissolved organic nitrogen and carbon. The fifth compartment of the REcoM-2 model consist the tracers of dissolved nutrient i.e. dissolved inorganic nitrogen (DIN), Dissolved silicate (DSi) and dissolved iron (DFe), dissolved inorganic carbon(DIC) and total alkalinity (TA) [Schourup-Kristensen et al., 2014]. REcoM-2 model also has sediment compartments for carbon, nitrogen, silica and calcium carbonate, that mainly consist of only the detritus sinking layer. Remineralization occurs in this compartment and by this process nutrients are restored to the water column [Schourup-Kristensen et al., 2014]. At the present model setup, the dissolution rate of $CaCO_3$ does not depend on saturation state but is described as a temperature dependent first-order dissolution reaction process [Yamanaka and Tajika, 1996].

From the Global Ocean Data Analysis Project (GLODAP) data set [Key et al., 2004] the RecoM-2, model initialization is done for the tracers of dissolved inorganic carbon (DIC) and total alkalinity (TA) [Schourup-Kristensen et al., 2014]. The tracers for DSi and DIN were set with values obtained from the data of Levitus World Ocean Atlas climatology of 2005 [Garcia et al., 2006]. PISCES model output was used as initialization for the iron field [Aumont et al., 2003] since no global observational field is available.

2.3.1 Processes that affect alkalinity and dissolved inorganic carbon in the model

The biological tracers (i.e. concentration of nutrients, biomass etc) are altered by the physics of the ocean through advection and diffusion and by biological processes in biogeochemical models. Every biogeochemical tracer in the model fulfills the mass balance. The rate of change

of the concentration for a given biological tracer T can be described by the following equation:

$$\frac{\partial T}{\partial t} = F_T + SMS_T \tag{16}$$

where F_T stands for the physical transport of the tracers by advection and diffusion and SMS_T stands for biological sources minus sinks, corresponding to the changes caused by biological processes.

For DIC and alkalinity, we have the following two equations for the SMS term [Hauck et al., 2013]. The sources for DIC are assumed respiration by diatoms, nanophytoplankton, and heterotrophs. The dissolution of calcium carbonate and remineralization of dissolved organic carbon (DOC) are also sources of DIC in the model [Hauck et al., 2013]. Formation of calcium carbonate and the fixation of carbon by primary producers are the sinks of DIC. Air – sea flux of CO_2 has also impact on surface DIC concentration.

$$
\begin{aligned}
SMS_{DIC} = & \ (r_{phy} - p_{phy}) \cdot C_{phy} + (r_{dia} - p_{dia}) \cdot C_{dia} + r_{het} \cdot C_{het} + \\
& \ \rho_{DOC} \cdot f_T \cdot DOC + \lambda \cdot CaCO_{3det} - calcification
\end{aligned}
\tag{17}
$$

here C_{phy}, C_{dia} and C_{het} are the carbon biomass of phytoplankton, diatoms and heterotrophs, respectively, r_{phy}, r_{dia} and r_{het} are the respiration rates of phytoplankton, diatoms and heterotrophs, respectively, p_{phy} and p_{dia} are the photosynthesis rates of phytoplankton and diatoms respectively, the remineralization of DOC is represented by ($\rho_{DOC} \cdot f_T \cdot$DOC) and λ is the calcite dissolution rate, which is explained below in more detail.

The alkalinity balance is determined by precipitation and dissolution of calcium carbonate, phytoplanktonic uptake of phosphate and nitrate, and remineralization of dissolved organic matter [Wolf-Gladrow et al., 2007]. Alkalinity is decreased during calcification and increased during the dissolution of $CaCO_3$. Phosphorus is taken into account assuming a constant ratio of N:P of 16:1. Alkalinity is increased by nitrogen assimilation and by the dissolution of calcium carbonate whereas production of $CaCO_3$ and dissolved organic nitrogen (DON) remineralization act as sinks.

$$
\begin{aligned}
SMS_{TA} = & \ (1 + 1/16) \cdot (a_{phy}^N \cdot C_{phy} + a_{dia}^N \cdot C_{dia} - \rho_{DON} \cdot f_T \cdot DON) + \\
& \ 2(\lambda \cdot CaCO_{3det} - calcification)
\end{aligned}
\tag{18}
$$

here a_{phy}^N and a_{dia}^N are the nitrogen assimilation rates by phytoplankton and diatoms respectively and the remineralization of DON is represented by ($\rho_{DON} \cdot f_T \cdot$DON).

In this study, two fundamentally different set up of dissolution rate have been used. One is that λ (in equation 17 and 18) has been set in such a way that the dissolution happens all

through the water column. In this case λ does not depend on saturation state but is described as a temperature dependent first-order dissolution reaction process [Yamanaka and Tajika, 1996]. Yamanaka and Tajika [1996] assume an exponential deacrese of the $CaCO_3$ sinking flux with depth, we reproduce this behaviour here by scaling λ with the sinking speed

$$\lambda = \lambda_0 \cdot \frac{w}{w(z = 0)} \tag{19}$$

In the other run we made λ dependent on Ω. This dependency can be described by using the following equation

$$\lambda = \lambda_0 \cdot \begin{cases} (1 - \Omega) & \text{for } \Omega < 1 \\ 0 & \text{for } \Omega > 1 \end{cases} \tag{20}$$

where λ = calcium carbonate dissolution rate

and Ω = local saturation state

2.4 GLODAP data set

We make use of a high quality global $1° \times 1°$ gridded mapped climatology data product: version 2 of the Global Ocean Data Analysis Project (GLODAPv2) [Lauvset et al., 2016] that contains the primary biogeochemical variables total alkalinity (TA), total dissolved inorganic carbon (DIC), temperature, salinity, nitrate, oxygen, phosphate, silicate, pH, and also $CaCO_3$ saturation states (Ω). The data set is merged from 724 scientific cruises during the years 1972 to 2013 that cover all the ocean basins including the Arctic Ocean. The ocean depth is divided into 33 standard layers in this climatology.

3 Model - data comparison

3.1 Distribution of DIC and alkalinity from observational data and the baseline model run for the present

Figure (5) shows the global dissolved inorganic carbon and alkalinity distribution at the ocean surface and at a depth of 3000 m from the GLODAPv2 data collection [Lauvset et al., 2016]. It is clearly seen from figure (5), that surface DIC has the lowest values near the equator and higher values towards the higher latitudes consistent with the higher solubility of CO_2 in cold water, but this feature is not completely uniform throughout the world ocean. The Pacific ocean surface has a lower value of DIC than the Atlantic and that fits with the fact that alkalinity is also

slightly higher in the Atlantic Ocean surface. Alkalinity has maximum values in the subtropics surface ocean, where salinity is also highest, because of evaporation. Due to the high values of alkalinity in the subtropical ocean surface, DIC also has a maximum there because with higher alkalinity, the ocean can store more carbon for the same atmospheric $p\text{CO}_2$.

At 3000 m depth, in general both DIC and alkalinity concentrations are higher than at the surface. The reason behind this is the biological pump which moves DIC away from the surface ocean into the deep ocean. The biological pump also has a small effect on the alkalinity as well (because the remineralization of organic matter also releases nitrate (NO_3^{2-}) and phosphate (PO_4^{3-}) but these are small compared to the effect on alkalinity from formation and dissolution of CaCO_3. The dissolution of CaCO_3 releases alkalinity in the deep ocean, leading to the observed increase with depth. Starting from deep North Atlantic, we have the lowest values
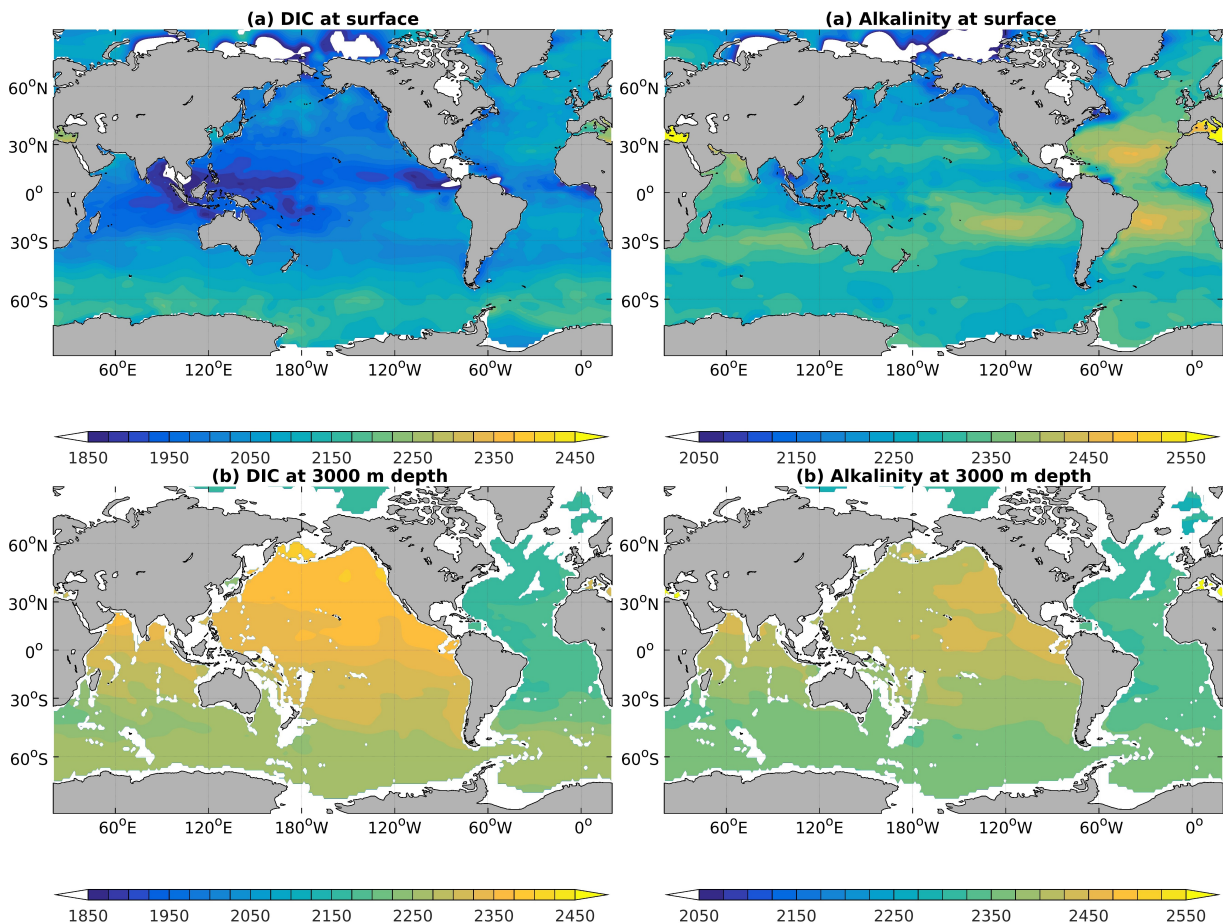
Figure 5: *Global distribution of dissolved inorganic carbon and alkalinity from observational data (GLODAP data, 2016 [Lauvset et al., 2016]); first row of the image represent the DIC and alkalinity at the surface denoted by (a) whereas (b) denotes at 3000 m depth in the ocean.*

at depth both in alkalinity and DIC. As we follow the conveyor belt out of the Atlantic Ocean into the Antarctic Circumpolar Current and then into the deep Pacific Ocean, both DIC and alkalinity increase. Water there has lost contact with the atmosphere for the longest time so

it has had the longest time to accumulate the remineralization products of organic carbon, and because of that DIC increases. Some dissolution of $CaCO_3$ also occurs here so there is also an increase in alkalinity along the conveyor belt. However, the gradient is less strong in alkalinity than DIC because there is more organic carbon raining down than $CaCO_3$. Figure (6) shows the
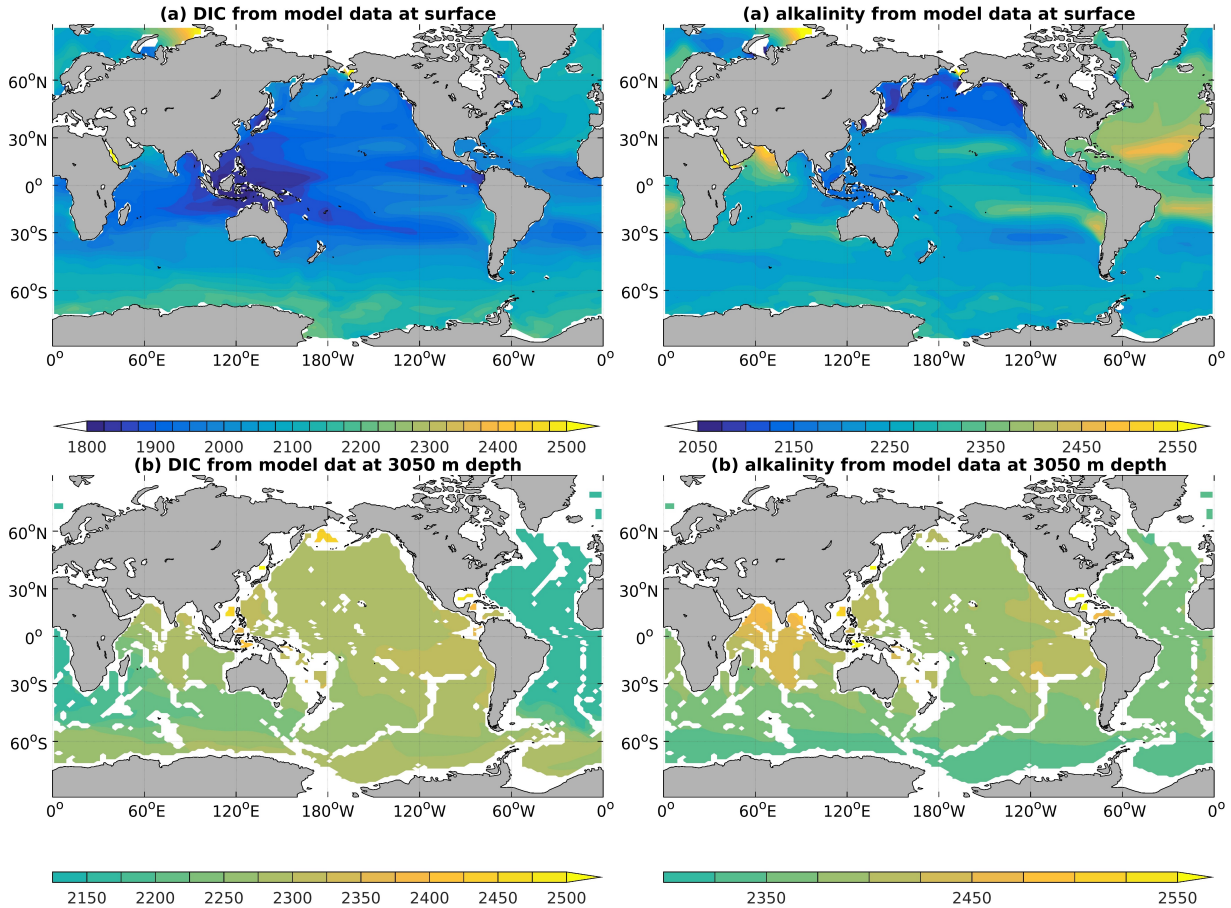

Figure 6: *Global distribution of dissolved inorganic carbon and alkalinity from model data set; first row of the image represent the DIC and alkalinity at the surface denoted by (a) whereas (b) denotes at 3050 depth in the ocean.*

global distribution of DIC and alkalinity from the model simulation. In general, the modeled data for DIC and alkalinity show quite similar patterns to the observational data, with low values at the surface and high in the deeper ocean. But the model data also shows some differences.

At the surface, the observational alkalinity in the South Atlantic and in the South Pacific seems to be slightly higher in the subtropics than in the model, especially in the southern hemisphere. At 3000 m depth, there is a strong gradient along the conveyor belt, with an increase along the conveyor belt both for DIC and alkalinity, so the general pattern is similar to observations. There is a difference in that the highest values in alkalinity in the deep ocean are found in the Indian Ocean in the model, while the maximum is distributed more broadly in the Indian and the Pacific Ocean for the observational data. This feature can be related to figure (8) from

the masters thesis [Vhuiyan, 2016], where he found that the model has relatively high CaCO$_3$ export production in the Indian Ocean. A possible explanation might be therefore that the alkalinity values in the deep Indian Ocean are caused by either a too low ventilation of this ocean basin or by a too strong calcification there.

In the case of DIC, it seems that the Atlantic values agree pretty well but that the increase along the conveyor belt is a little bit weaker than in the observations. This pattern is similar for alkalinity values. Therefore the question is, what the reason behind this feature might be. Is it more a circulation feature or a feature of the biological production? The export of organic carbon in the model is roughly 10 Pg C yr^{-1} [Vhuiyan, 2016], which agrees with current estimates. So it is pretty clear that we do not have too little export of organic matter. Another reason could be that the distribution of remineralization over depth in the model differs from that in reality. The flux of organic carbon decreases with depth due to remineralization that happens while the organic particles sink, and we also do not know whether the model describes that very well or not. Figure (5) and (6) represent the data only at the surface and at 3000 m depth, so from them we do not know anything what is happening in between.

Figure 7: *Global average vertical profile of DIC from observational and model data; DIC form observational data denoted by (a) whereas (b) denotes the model data value.*

Figure (7) shows the global average vertical profile of dissolved inorganic carbon (DIC) from both observational and model data. It is clearly seen that in both, at the surface DIC is reduced and then increases with depth. In the observed data, the DIC increase with depth is

strong in near the surface and decreases with depth; DIC gets almost uniform below 1500 m depth. In the model, there is an intermediate maximum where the dissolved inorganic carbon gets higher than the observations around 800 m to 1200 m depth. At depths larger than 2000 m, modeled DIC gets lower than observed. This is an indication that remineralization occurs too high in the water column and leads to an overestimate at mid - depth and on underestimate at depth.
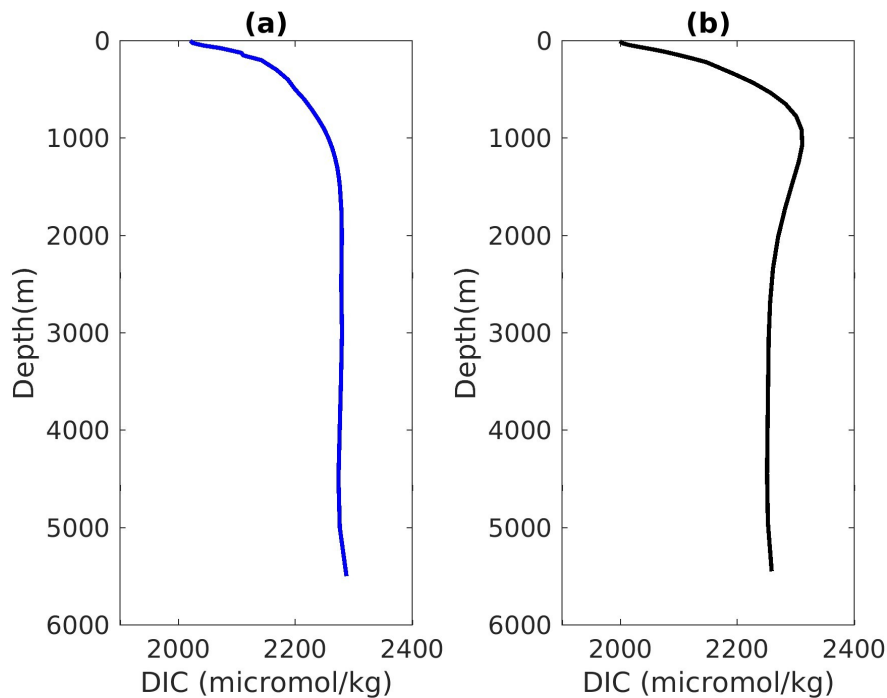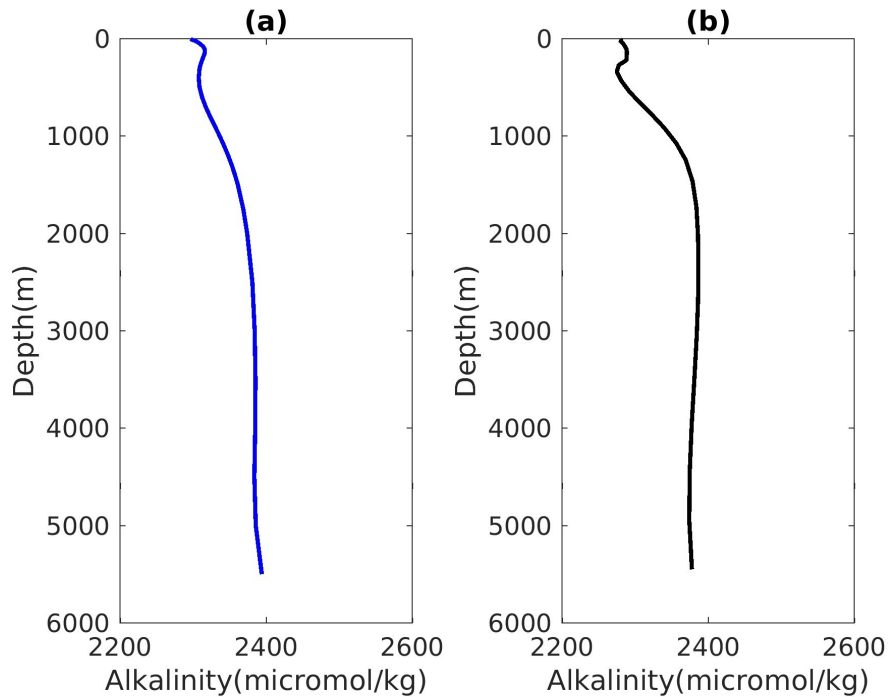

Figure 8: *Global average vertical profile alkalinity from observational and model data; alkalinity form observational data denoted by (a) whereas (b) denotes the model data value.*

The global average vertical profile for alkalinity is shown in figure (8). Alkalinity values show similar features as DIC but much weaker with lower values near the surface with a small intermediate maximum and an increase with depth in between 1000 m to 4000 m. Surface values in the model are pretty close to observations, but also have a little bit too much increase in mid-depth around 1200 m to 2000 m. This might also be an indication that too much dissolution of $CaCO_3$ is happening at that depth range.

3.2 Saturation state of CaCO$_3$ from observational and model data

The saturation state of calcium carbonate (Ω) both from observational and model data are shown in figure (9) at the surface and at 3000 m depth. From this figure, it can be said that the saturation state of CaCO$_3$ is higher at the surface than in the deep ocean. At the surface it is high in the subtropical regions and lower towards the high latitude. These features are almost uniform all over the world ocean. At 3000 m depth, the Atlantic Ocean shows slightly higher Ω values than the Pacific Ocean. The reason for this is then, along with the conveyor belt the alkalinity increases not as much DIC (the alkalinity always larger than DIC). So the difference between alkalinity and DIC is larger in the Atlantic than the Pacific. To a good approximation the difference between alkalinity and DIC is the concentration of CO$_3^{2-}$. So the carbonate ion concentration decreases from the Atlantic towards the Pacific as DIC increases.

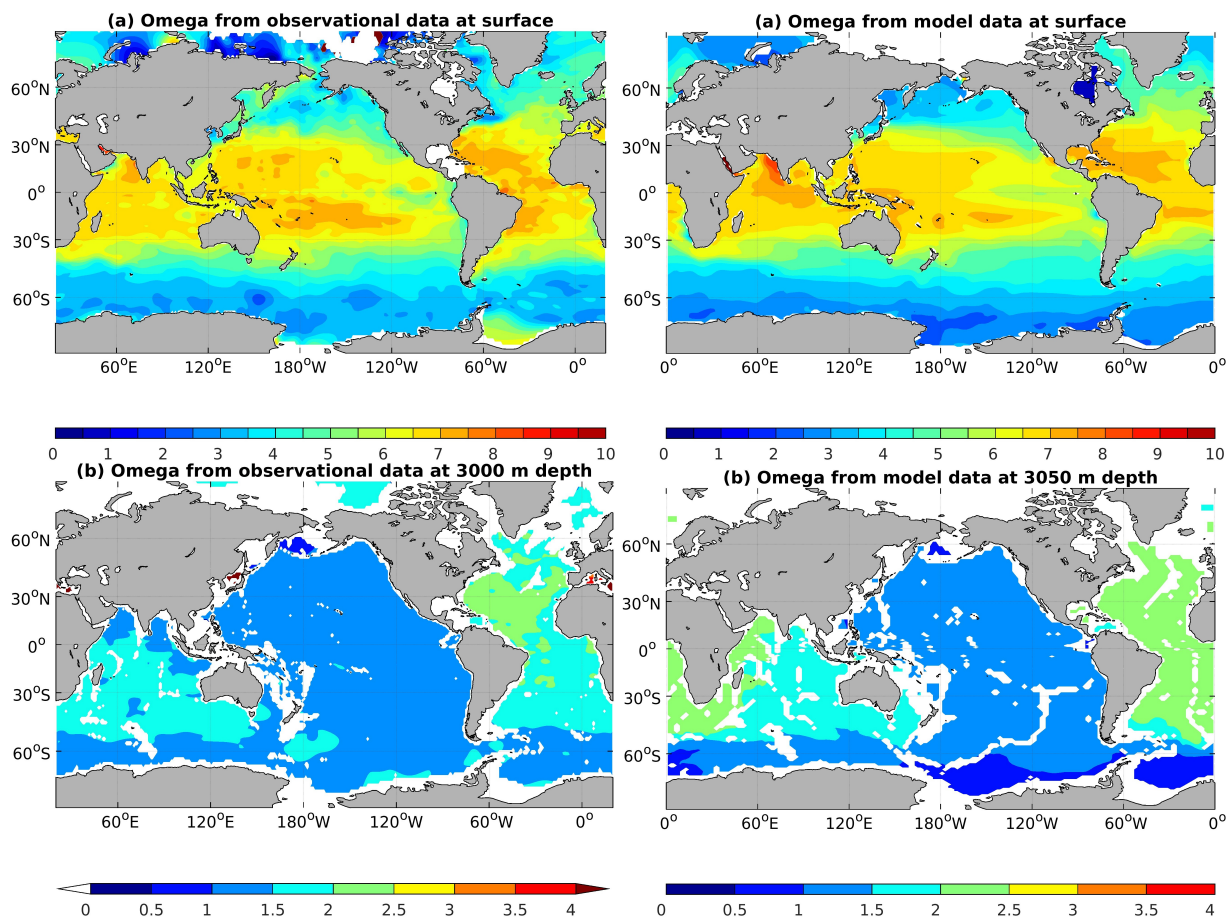Figure 9: *Global distribution of saturation state (Ω) from observation and model data; first row of the image represent the value at the ocean surface denoted by (a) whereas (b) denotes at the deeper ocean.*

Surface omega value from the model simulation shows a higher value in the red sea and slightly higher value in the northern subtropics region of Indian Ocean in comparison to obser-

vational data. In the deeper ocean, the model shows slightly higher values than the observations in the Atlantic Ocean and the Indian Ocean where the Pacific Ocean shows quite similar pattern.

The calculation of Ω should take into account the nutrients though nutrients concentration are neglected in this study because of their small effect on alkalinity [Orr and Epitalon, 2015]. The approximation that is used in this study for the calculation of Ω from DIC and alkalinity may create an error of Ω distribution in the deep ocean where nutrients are high. On the other hand, the surface ocean is not affected by nutrient concentration because here the nutrient concentrations are in general small except in the Southern Ocean.

4 Changes with LGM and present

To investigate the physical and biogeochemical changes between the LGM and present day, a model simulation for the LGM, with atmospheric forcing taken from coupled ocean-atmosphere simulations performed with COSMOS [Zhang et al., 2013], has been done (EXP 03). The simulation has come close to an equilibrium condition after 3000 years of integration time. Over the last 100 years of the integration time (years 2900 - 3000), average ocean temperature decreased by -0.01° C and the average ocean carbon content decreased by -0.441 μmol/L.

4.1 Physical changes

4.1.1 Atlantic overturning circulation
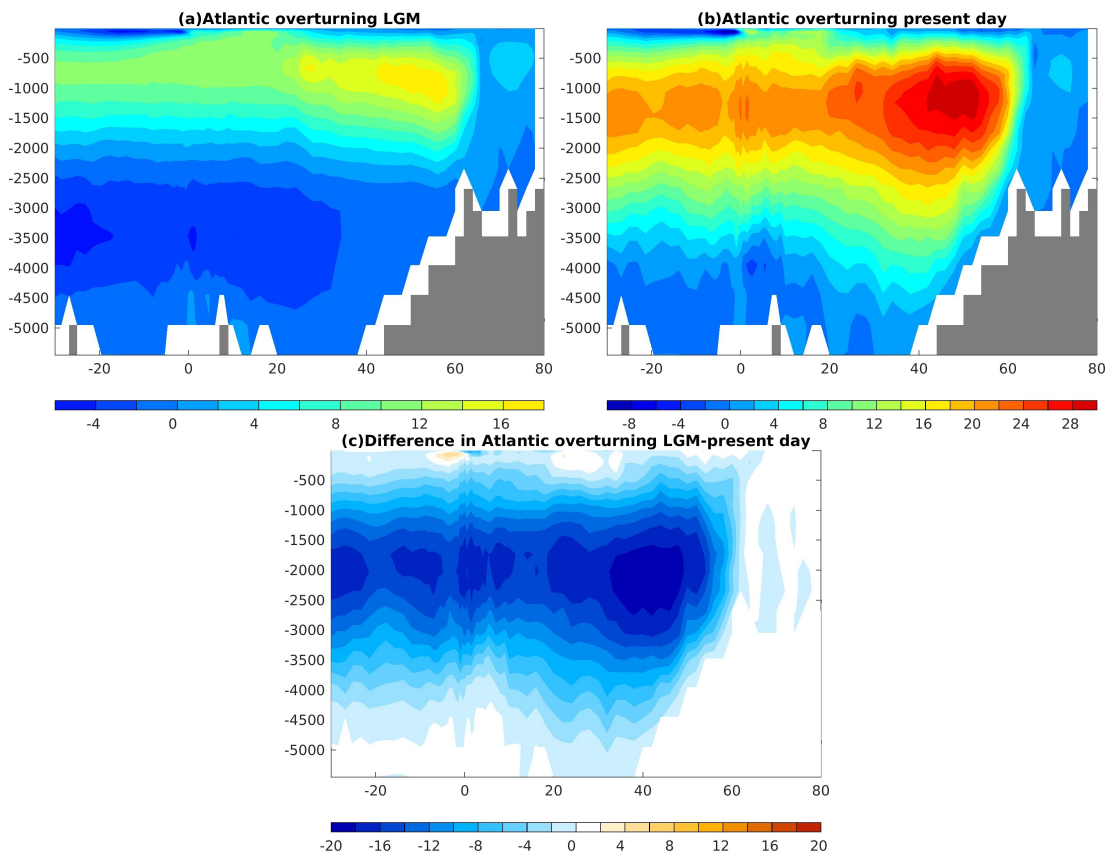
Figure 10: *Atlantic overturning streamfunction for LGM (a) and present day climate (b) and difference between them shown by figure (c).*

The changes observed in the Atlantic ocean between the LGM and present day climate are connected to changes in the Atlantic meridional overturning circulation (AMOC) which is characterized by a northward flow of warm, salty water in the Atlantic upper layers to supply the formation of North Atlantic Deep Water (NADW), one of the primary overturning cells,

and a southward flow of colder water in the deep Atlantic in which Antarctic Bottom Water (AABW) flows northward below depths of about 3,500 m and gradually rises into the lower part of the southward-flowing NADW [Delworth et al., 2008]. The Atlantic meridional overturning streamfunction for LGM and present day model runs are presented in figure (10). LGM AMOC is weaker and shallower than in the present day and has a maximum transport of 17.7 Sv for LGM where present day transport is 29.8 Sv. This is roughly consistent with the model results from [Völker and Köhler, 2013]. The weakened glacial AMOC is also associated with a shoaling of its lower boundary approximately from 3500 to 2000 m as Glacial North Atlantic Intermediate Water (GNAIW) due to the enhanced northward invasion of Antarctic Bottom Water (AABW). As a result, much of the Atlantic Ocean below 2000 m is dominated by Antarctic Bottom Water (AABW) as part of the lower overturning cell. These changes in the lower and upper overturning cells are conducive to the development of a global overturning circulation dominated by a denser AABW and a shallower AMOC. This shoaling depth of NADW is similar with [Buchanan et al., 2016b] where they mentioned that the the LGM NADW was lowered by approximately 3000 to 1500 m from present day.

4.1.2 Atlantic zonal mean temperature and salinity

Figure (11) shows a meridional section of the zonal average temperature and salinity for both LGM and present day simulations and also the difference. Most of the Atlantic ocean in the LGM is cooler than at the present day. LGM NADW is getting much colder than the present day but AABW is not getting so much colder because it is already near freezing temperature.

On average the present day Atlantic ocean temperature is approximately 4° C higher than the glacial ocean. The LGM surface temperature ranges from approximately 23° C to -2° C while the present day surface temperature is from approximately 28° C to -1° C. The average surface temperatures are approximately 11° C and 14° C respectively. In the deep ocean, at 3050m depth, the LGM ocean temperature, range from approximately 0.23° C to -2° C where the present day temperature is from approximately 5° C to 0.1° C. The average deep ocean temperatures are approximately -1° C and 3° C respectively.

LGM salinity increases all over the ocean in the LGM because of less water in the ocean but the increases are not equally distributed. LGM Antarctic intermediate water remains relatively fresh and gets shallower but Antarctic Bottom Water gets more salty. The AABW becomes more salty in the LGM mainly due to the increase of the brine release associated with the formation of sea-ice. AABW forms under the regions of year-round sea-ice cover. The associated sea-ice melting and growth results in a vertically asymmetric redistribution of salt in the ocean,
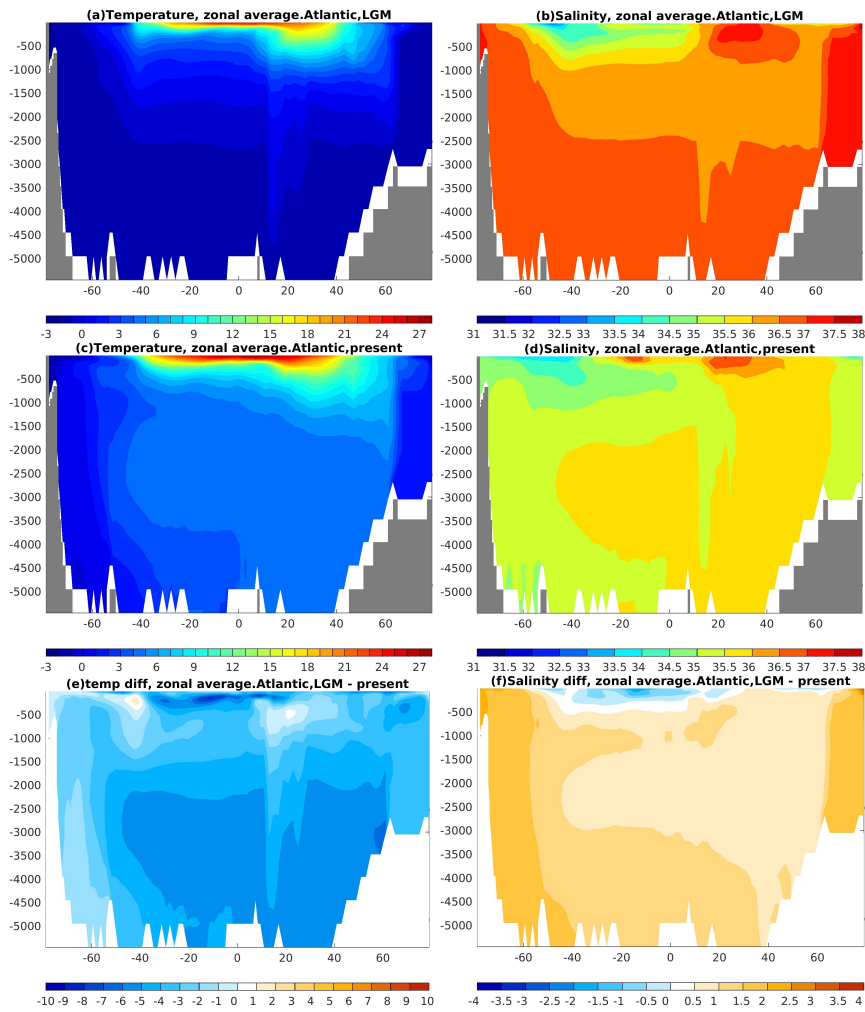
Figure 11: *Zonally averaged temperature (a and c) and salinity (b and d) and the difference in temperature(e) and salinity(f) within the Atlantic basin over LGM (a and b) and present day (c and d).*

transporting more salt from the surface to the deep-ocean. These results are in agreement with the recent reconstruction by pore fluid measurements of the glacial salinity and temperature in sediment cores [Adkins et al., 2002].

In the present day ocean, both Antarctic intermediate water and Antarctic Bottom Water (AABW) are relatively fresh but the NADW is relatively more saline penetrating southward into the Southern Ocean and leading to a reversal of the salinity stratification in the abyss [Talley, 2013]. The associated overturning streamfunction (figure 10.b) reveals that this salinity feature is associated with NADW that flows southward as part of the Atlantic meridional overturning circulation (AMOC). Compared with LGM to present day, most of the region are high in salinity except at the surface in the subtropics, caused by high evaporation in the subtropics. Atlantic LGM salinity is approximately 1 psu higher than the present day on average. Present day Atlantic surface salinity varies from 37.03 to 33.69 psu where LGM surface salinity ranging

from 37.70 to 32.83 psu. In the deep Atlantic, present day salinity values range from 35.67 to 35.01 psu where LGM maximum and minimum are approximately 37.38 to 36.4 psu.

4.1.3 Pacific zonal mean temperature and salinity

Zonal average Pacific Ocean temperature and salinity are shown in figure (12) both for LGM and present day. Temperature and salinity in the Pacific ocean shows a much more uniform pattern than the Atlantic ocean, especially a more cooling in the deep Pacific than the Atlantic because in the Pacific there is no Deep Water formation like in the Atlantic ocean. LGM pacific
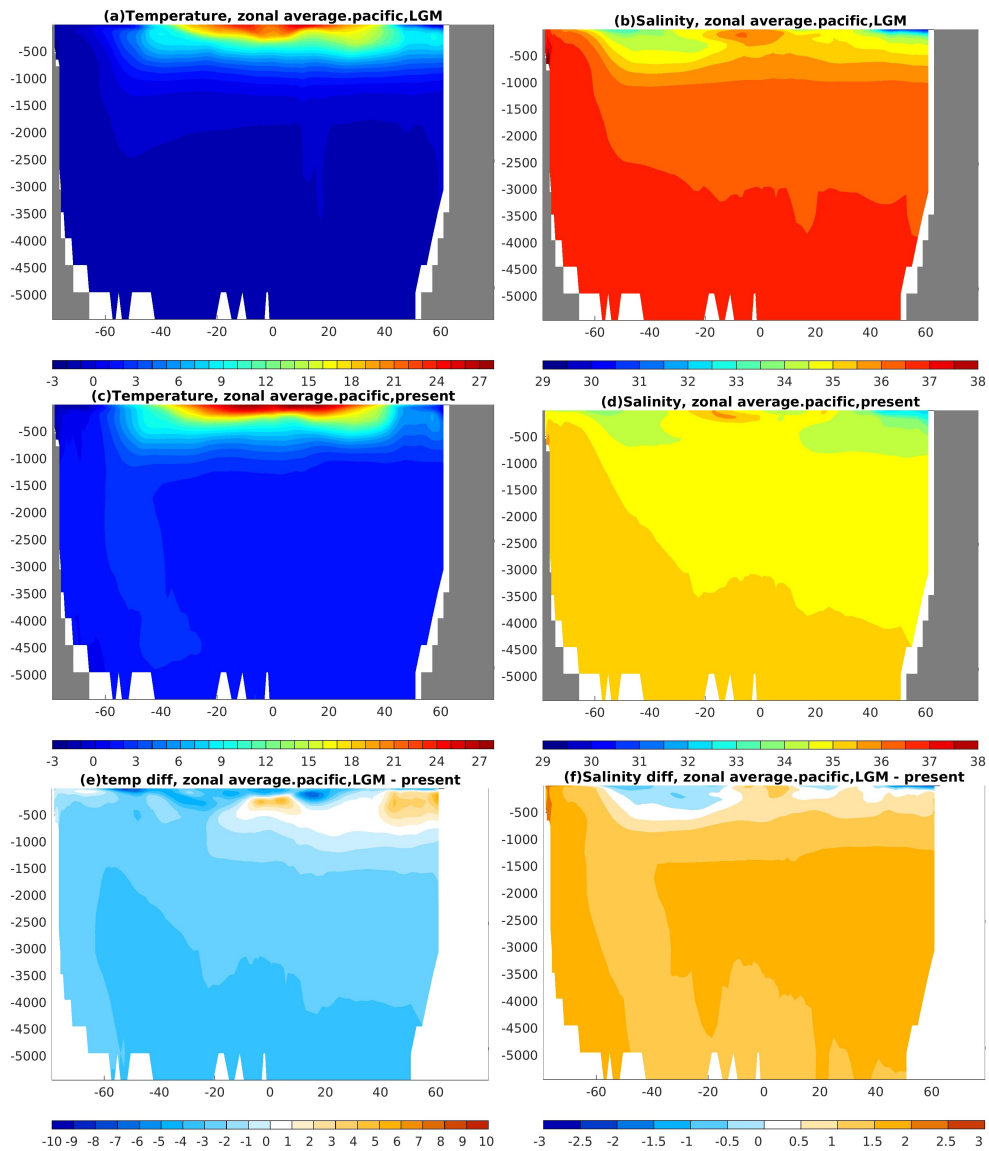

Figure 12: *Zonally averaged temperature (a and c) and salinity (b and d) and the difference in temperature(e) and salinity(f) within the Pacific basin over LGM (a and b) and present day (c and d).*

deep water is cooler than at present day but the temperature difference is not that much as

24

surface because Pacific deep water is already much colder. North Pacific Intermediate Water (NPIW) is deeper in the LGM than in the present day which leads to the pattern of increased LGM temperature around 500 m depth in the upper North Pacific.

Modeled average LGM Pacific temperature is approximately 2° C lower than at the present day. But the lower thermocline in the North Pacific shows higher temperature for the LGM because of deeper NPIW whereas LGM Pacific averaged surface temperature is around 3° C cooler than at the present day. The LGM Pacific surface temperature ranges from approximately 25° C to -2° C where the present day surface temperature is from approximately 28° C to -1° C. Figure (12 b and d) shows the salinity in the Pacific ocean for the LGM and present day respectively. The Pacific deep ocean water for present and LGM climate show a similar trend i.e. both are more salty than the surface. But the LGM Pacific ocean is higher in salinity at the surface as well as at the deeper part than the present day. From the salinity difference plot between LGM and present day (figure 12.f), it is clear that the LGM Pacific ocean is more salty than the present day except some freshening of thermocline waters (AAIW and surface waters) in the south Pacific.

4.1.4   Maximum sea ice extent
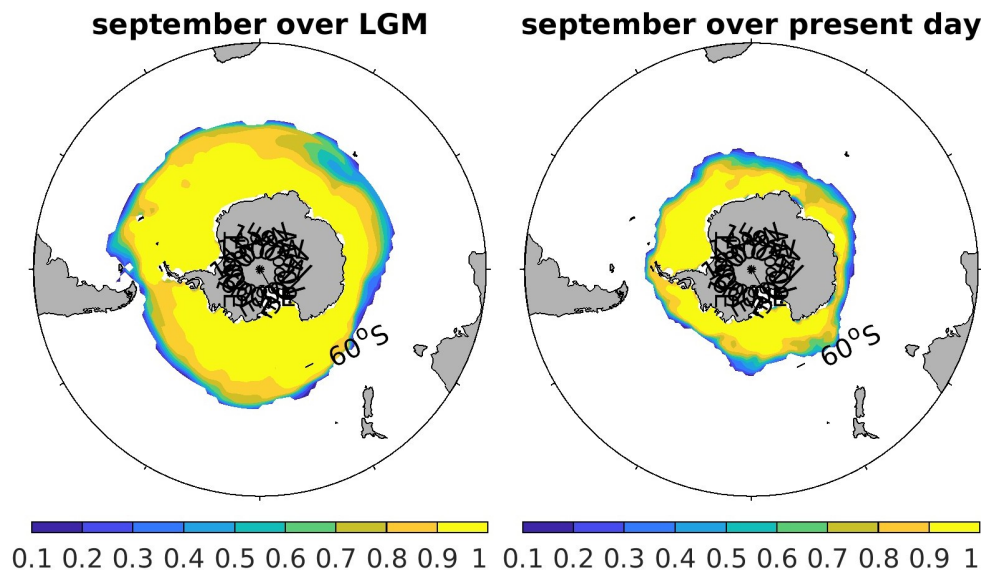

Figure 13: *Fractional sea ice cover maximum (september average) in the LGM (left) and present day (right).*

The average sea ice extent for september over LGM and present day is presented in figure (13). Associated with colder sea surface temperature(SST), sea ice coverage (fractional sea ice area) is expanding in the LGM (for both hemispheres) compared to the present day. The

maximum sea ice-covered area is 33.7×10^6 km^2, more than twice the area in the present day simulation (11.9×10^6 km^2), and even in Southern hemisphere (SH) summer an area of 28.6×10^6 km^2 remains ice covered, compared to only 0.8×10^6 km^2 in the present day model simulation. During the LGM, the model produces a stronger seasonal cycle of sea ice area than at the present day. The northward expansion of sea ice around the Southern Ocean and Antarctica matches well with proxy reconstructions [Gersonde et al., 2005] and also with other model simulations [Buchanan et al., 2016a, Völker and Köhler, 2013]. Maximum sea ice extent ranged as far north as 47° S in both the Atlantic and Indian regions [Gersonde et al., 2005] and as far north as 55° S in the Southern Ocean Pacific region [Benz et al., 2016, Gersonde et al., 2005].

4.2 Biogeochemical changes

4.2.1 Atlantic zonal mean alkalinity and DIC

The Atlantic distribution of alkalinity and DIC for the LGM, present day and their difference are shown in figure 14. Both the LGM and present day simulations show a qualitatively similar pattern of alkalinity distribution with the lowest value found in southern hemisphere surface ocean and Antarctic Intermediate Water and highest value in the deep ocean. Both for the LGM and present day, deep Atlantic ocean has higher alkalinity concentration than the surface ocean. The lower alkalinity concentartion in waters shallower than 500 m is resulting from the biological production of CaCO$_3$ while the higher alkalinity values in the deep ocean results from the dissolution of CaCO$_3$. The alkalinity distribution of the Atlantic ocean is also controlled by factors that govern salinity [Broecker and Peng, 1982, Millero et al., 1998].

In comparison to the present day, the LGM ocean is more alkaline at the ocean depth as it is more saltier than the present day (figure11.f). In the LGM, Antarctic bottom water (AABW) is getting more salty and also alkaline and NADW (less salty than AABW) is partly replaced by AABW. LGM alkalinity concentration is ranging approximately from 2690 to 2160 mmol/m^3 where the present day ocean alkalinity concentration is from 2480 to 2283 mmol/m^3. On average LGM ocean is higher in alkalinity concentration by approximately 45 mmol/m^3. LGM Atlantic surface ocean has lower alkalinity concentration is about to 23 mmol/m^3 whereas the deep ocean (3500m depth) is higher in concentration by approximately 115 mmol/m^3 than the present day. A high alkalinity difference is observed at the deep Atlantic in the more salty and isolated Caribbean sea.

In general both the glacial and present deep Atlantic ocean is enriched in DIC compared

Figure 14: *Zonally averaged alkalinity (a and c) and DIC (b and d) and the difference in alkalinity (e) and DIC(f) within the Atlantic basin over LGM (a and b) and present day (c and d).*

to the surface ocean. For the present day, Antarctic Intermediate Water is relatively enriched in DIC partly because it comes from the Southern Ocean where DIC concentration is high and partly because of remineralization of organic matter. This tendency is getting stronger in the glacial ocean.

Glacial Atlantic oceanic concentration of DIC is on average approximately 24 mmol/m^3 less than in the present day simulation. This carbon loss is probably related to the effect of physical changes in the ocean which include a number of effects that can have opposing effect on CO_2 like expansion of sea ice area, solubility increases due to cooling, overturning circulation change and the tendency of outgassing because of lower pCO$_2$. Less concentration of DIC is observed in the LGM surface ocean because of lower pCO$_2$ at the LGM surafce. The increase of DIC

in deep water masses is associated with the replacement of relatively carbon poor NADW by carbon richer Antarctic bottom water.

Both LGM and present day ocean are also high in DIC at the equator in the depth between 500 to 1000 m because of the production of organic matter at the equator. The strength of this pattern has increased in the LGM ocean. Phytoplankton produces organic matter by the uptake of carbon dioxide, this organic matter is then transported to deeper layers and increases DIC when its remineralized at depth (biological pump).

Comparing the difference plot of alkalinity (14.e) and DIC (14.f), the LGM deeper ocean is generally high in alkalinity and DIC except south of 60° S. In this latitude alkalinity increases but DIC decreases throught the whole water column. One reason behind this decoupling is less biological production in high southern latitude in the glacial ocean and less organic carbon transport from the surface down deep into the ocean. Another reason is the lower glacial surface $p\text{CO}_2$ in general.

4.2.2   Pacific zonal mean alkalinity and DIC

Figure (15) shows the distribution of alkalinity and DIC in the Pacific Ocean for the LGM, the present day and also their differences. Both the LGM and present day Pacific Ocean show a qualitatively similar pattern of alkalinity and DIC distributions. Both LGM and present day Pacific Ocean alkalinity concentration at the depth $\sim$ 0 to 1000m is lower than in the deeper ocean. Deep ocean alkalinity increases towards the North Pacific which contents the oldest water.

The DIC concentration is also generally lower in the surface than in the deeper ocean. Unlike for alkalinity, the maximum concentration of DIC in the North Pacific is found at intermediate water depths between 1000 - 2000 m. Both deep DIC and alkalinity are higher in the Pacific than in the Atlantic (both for LGM and present day) because they get enriched over time as deep water spreads Atlantic into the Pacific with the conveyor belt circulation.

In the present day, the lowest DIC and Talk concentrations in the Pacific are observed in surface waters. Surface DIC ranges approximately from 2236 to 1934 mmol/m^3 where alkalinity varies from 2360 to 2159 mmol/m^3. These variations in surface ocean carbonate concentrations are correlated with salinity. Circulation plays an important role to the distribution of DIC and alkalinity in the upper 1000m depth. Below North Pacific Intermediate Water (NPIW), alkalinity concentrations increase to a large maximal at approximately 1500 – 3500 m depth. Total alkalinity concentrations range from 2160 – 2474 mmol/m^3. The differences between the DIC and alkalinity, specially in intermediate waters, are caused by in-situ re-mineralization. The DIC is
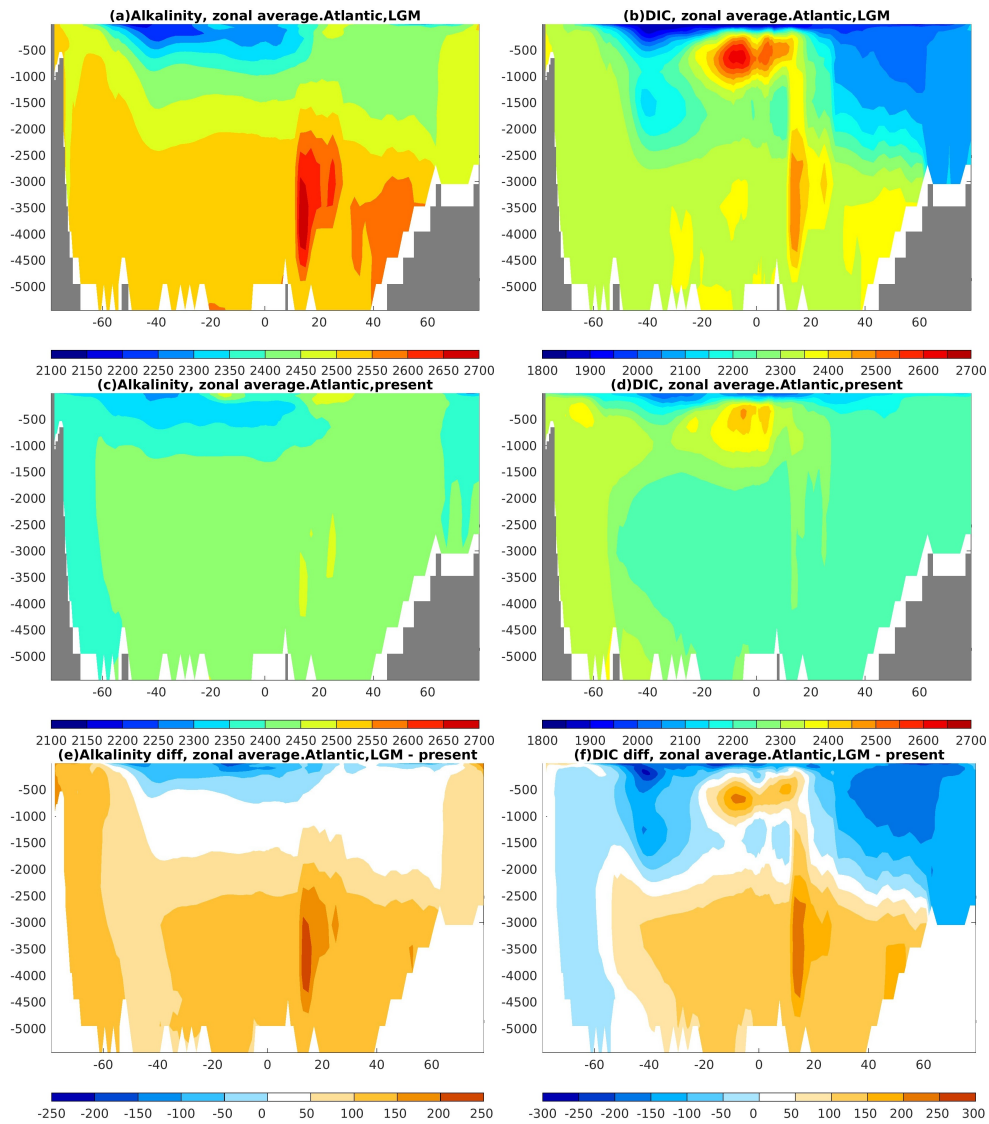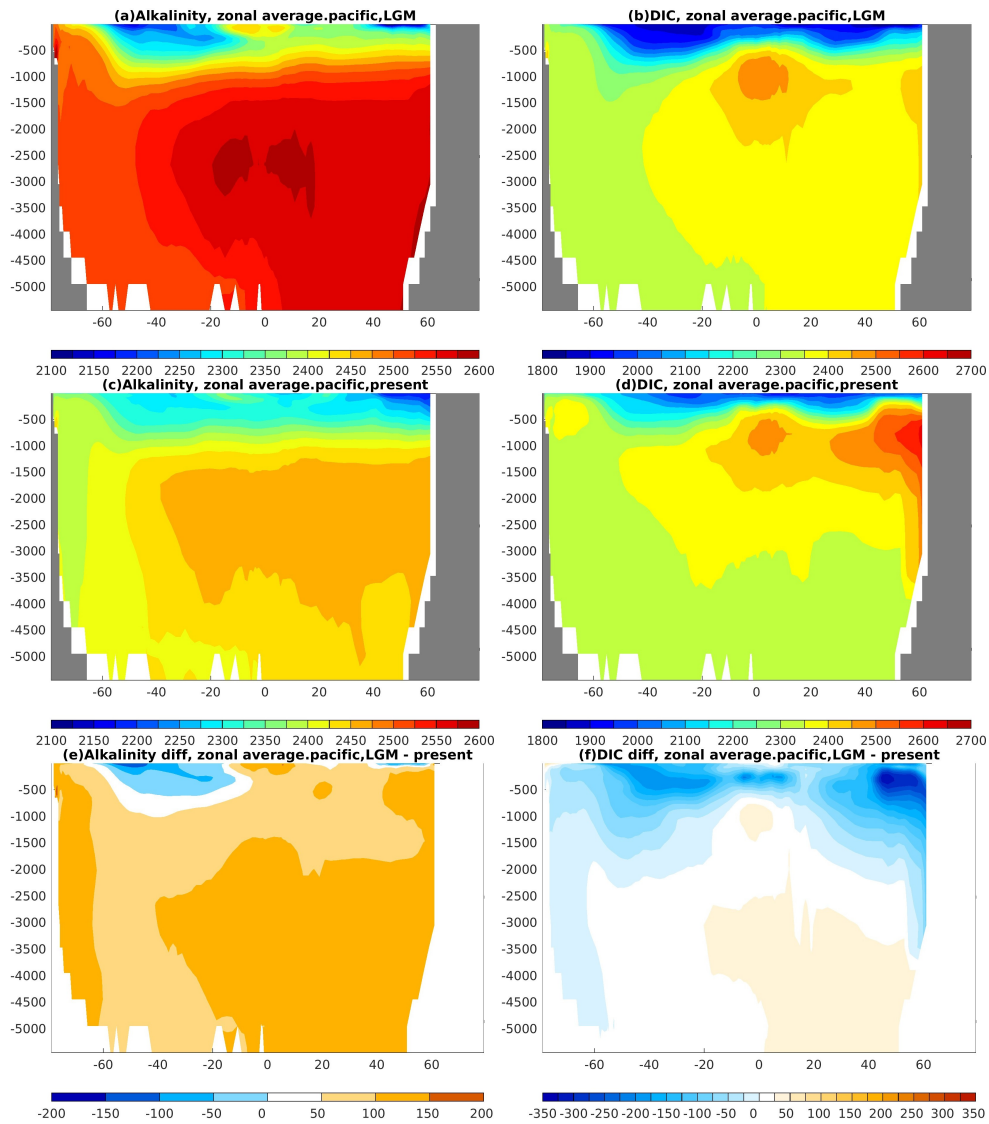
Figure 15: *Zonally averaged alkalinity (a and c) and DIC (b and d) and the difference in alkalinity (e) and DIC (f) within the Pacific Ocean basin over LGM (a and b) and present day (c and d).*

shallower than the alkalinity because the total inorganic carbon is highly influenced by the shallow re-mineralization of soft tissue organic matter, where the alkalinity is strongly influenced by the deeper calcium carbonate particles dissolution in the water column[Chen, 1990].

LGM Pacific ocean alkalinity and DIC concentrations are also qualitatively similar with present day pattern i.e. low at surface and high at ocean depth. Most part of the LGM Pacific ocean is quite substantially higher in alkalinity than in the present day except in AAIW, which is getting fresher (= less alkaline). DIC Pacific concentration in the LGM is higher in the deeper ocean and lower in the surface. DIC increases in the deep ocean below ~ 2500 m except in the Southern Ocean where it deacreses while alkalinity increases. This pattern is similar to the pattern in the Atlantic.

4.3 Discussion

It is clearly observed from the description of chapter 4.2, that there are changes in the distribution of alkalinity and DIC between the LGM and present day model run both in the Atlantic and Pacific Ocean. Many factors can govern these changes: higher overall salinity and alkalinity of the ocean in the LGM changes, changes in the location of different water masses, changes in biological production, ocean temperature leading to changes in solubility of CO_2, atmospheric pCO_2 etc.
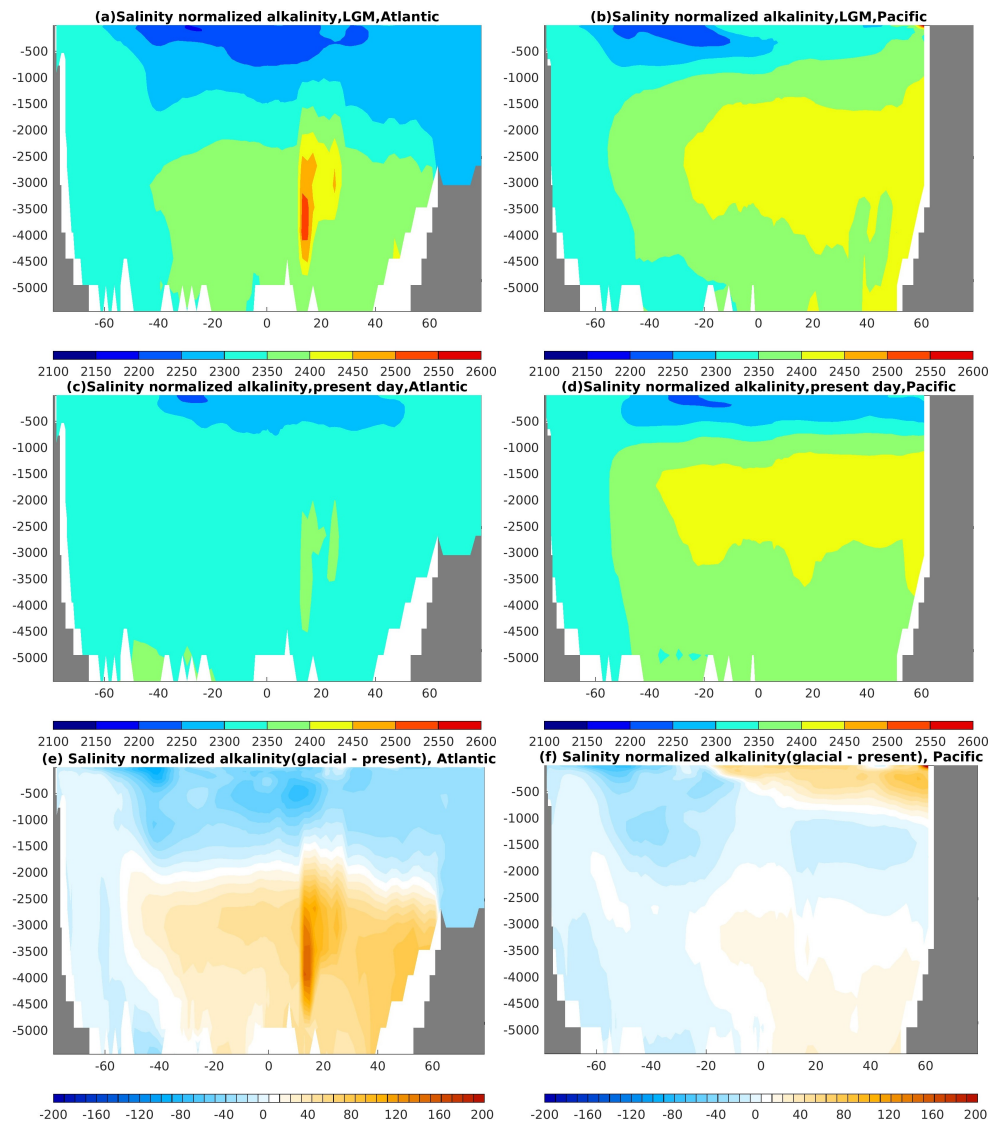
Figure 16: *Zonally averaged salinity normalized alkalinity within the Atlantic Ocean (a and c) and Pacific Ocean basin (b and d) between LGM and present day; (a and b) represent the salinity normalized alkalinity over LGM whereas (b and d) represent over present day and difference between them in the Atlantic shown by (e) and in the Pacific basin shown by (f).*

To remove the effect of evaporation and precipitation (i.e.,the hydrological cycle effect) a

salinity normalization on alkalinity (Alk_1) is done by converting each alkalinity (Alk) measurement to its expected value at a salinity (S) of 35 using equation (21) [Millero et al., 1998].

$$Alk_1 \quad = \quad \frac{Alk \times 35}{S} \tag{21}$$

The LGM and present day salinity normalized alkalinity (Alk_1) (fig 16. a – d) shows a similar pattern with the normal alkalinity (Alk) in the Atlantic (fig 14. a and c) and Pacific Ocean (fig 15. a and c) is lower at the surface and high at the deep ocean. The overall Alk_1 concentration is lower than the normal alkalinity (Alk).

The Alk_1 difference plot between LGM and present day Atlantic Ocean shows that the LGM Alk_1 concentration is lower at the depth range in between $\sim$ 0 - 2000 m but higher at the deeper ocean than the present day. Also the whole water column south of 60 $^\circ$ S shows a lower ALK_1 concentration. In the surface ocean, the distribution of Alk generally matches that of salinity because Alk in the open ocean is mainly controlled by salinity changes [Lee et al., 2006; Millero et al., 1998]. Maximum Alk_1 concentration in the Pacific Ocean is observed in the NPIW which is the region and the very most deeper ocean. The most northwestern part of NPIW is more freshest and most oxygenated part, this suggest that region is the source of NPIW for the subtropical gyre [Talley, 1993]. The LGM and present deep Atlantic and Pacific
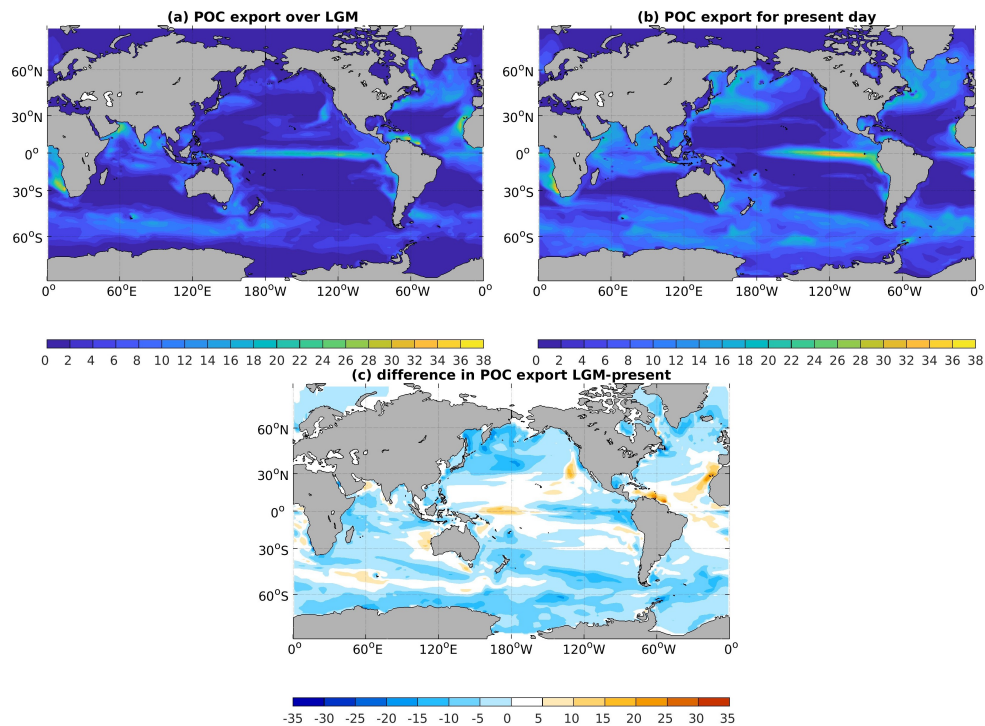

Figure 17: *Sinking flux of particulate organic carbon (POC) over 100 m depth for the LGM (a) and present day (b) and difference between them shown in (c).*

Ocean chemistry can be distinguished from each other by the formation of freshly ventilated

31

deep water in the Present day North Atlantic Ocean, which was more homogeneous during glacial time [Lea, 1993, Boyle, 1992, Duplessy et al., 1988, Curry and Lohmann, 1982]. From the salinity normalized alkalinity plot one can see that the location changes of different water mass is an important factor. Along with the location changes of different water mass between LGM and present day their salinity also changes. The most prominent example is the larger volume of AABW in the Atlantic which at the same time gets saltier.

The lower surface Alk_1 is governed by the production of $CaCO_3$ where the deeper high concentration Alk_1 is dominated by the high dissolution rate of $CaCO_3$. $CaCO_3$ produced at the surface ocean and start to dissolve when it leaves the productive upper layer of the ocean as upper layer is supersaturated with respect to both mineral phase of $CaCO_3$ whereas deep waters are undersaturated.

The overall Alk_1 distribution shows that an important factor in the change of ALK is the extended volume of AABW in the LGM. But the deacrease of Alk_1 in the upper 2000 m and throughout the water column in the Southern Ocean as well as the increases of Alk_1 below 2000 m in the rest of the ocean point to changes in the vertical flux of POC and $CaCO_3$ as further factors. Figure 17 and 18 shows the sinking flux of POC and $CaCO_3$ and also the differences
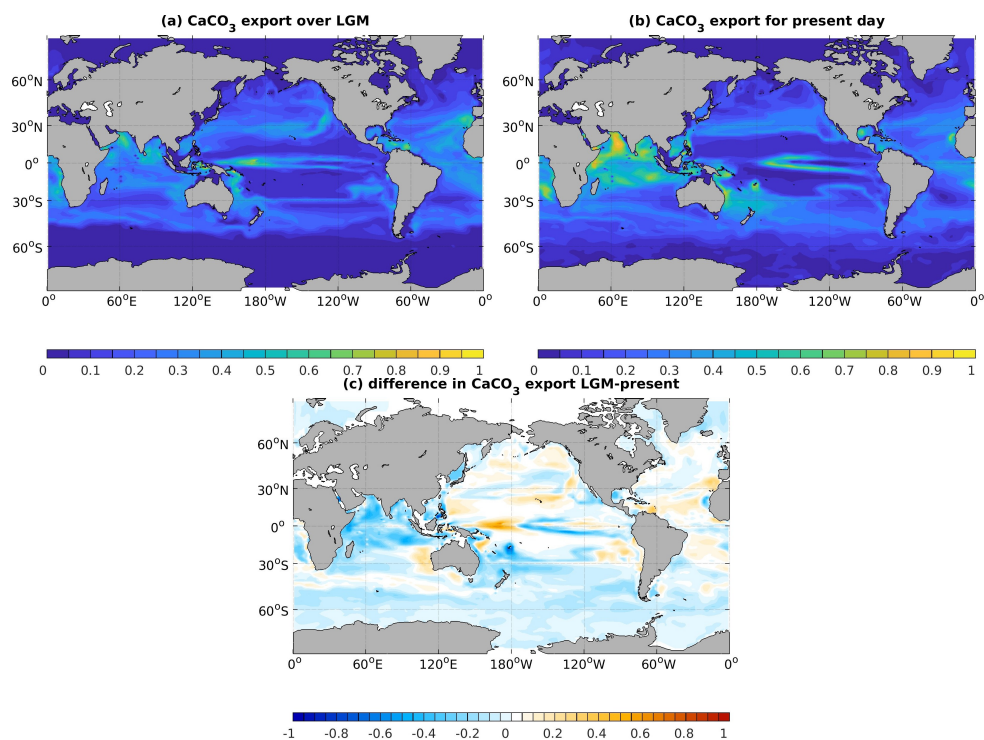

Figure 18: *Sinking flux of calcium carbonate ($CaCO_3$) over 100 m depth for the LGM (a) and present day (b) and difference between them shown in (c).*

between LGM and present day. The LGM POC export is higher mainly in the tropical region

of the Atlantic Ocean, east equatorial and northern subtropics of the Pacific Ocean, the area of high productivity due to upwelling. The subtropical regions are oligotrophic i.e., nutrient poor so that there is not much export of organic carbon. Enhanced productivity is also detected in the subpolar regions in the Atlantic and the North Pacific, around Antarctica and throughout the north Indian Ocean mostly driven by diatoms. The overall calculated POC export (6.830 Pg C yr^{-1}) is lower in the LGM than the present day (9.647 Pg C yr^{-1}).

The maximum $CaCO_3$ export mostly occurs at the boundaries between high nutrient and low nutrient conditions, e.g. at the boundaries of equatorial upwelling. The subpolar regions, where much POC export happens, are regions of less $CaCO_3$ export. The maximum export of $CaCO_3$ is found in the Indian Ocean. LGM $CaCO_3$ export also higher at the tropical region of Atlantic Ocean, eastern equatorial Pacific Ocean than the present day. The glacial model run calculates a total export of $CaCO_3$ of 0.281 Pg C yr^{-1} which is lower than the present day (0.342 Pg C yr^{-1}).
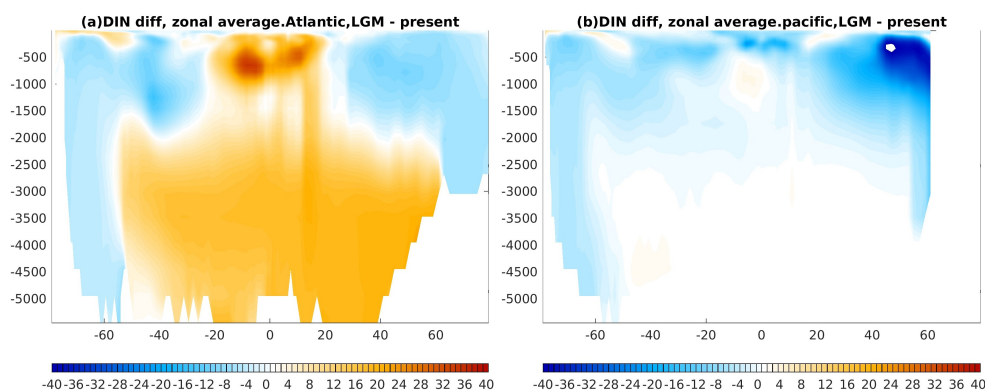
Figure 19: *Zonally averaged differences in dissolved inorganic nitrogen (DIN) within the Atlantic (a) and Pacific basin (b) over LGM and present day.*

The changes of POC export is also reflected in the dissolved inorganic nitrogen (DIN) distribution differences (figure 19). Figure 19 shows the difference in dissolved inorganic nitrogen (DIN) between the LGM and present day over the Atlantic and Pacific Ocean. The mid depth changes in DIC in the tropics is consistent with DIN distribution. They are driven by a high biological production with more export of organic carbon in the tropical Atlantic than the Southern Ocean.

5 Changes due to omega dependency to calcite dissolution

Two further model simulations (EXP 02 and EXP 04, table 1) with a dependency of dissolution of $CaCO_3$ on the saturation state (Ω) have been done for present day and LGM. The aim is to see how alkalinity, DIC and saturation horizon vary from the previous model runs where dissolution was not dependent on Ω. Between EXP 01 and EXP 02, and between EXP 03 and EXP 04 model runs the only thing that changes is $CaCO_3$ dissolution. Changes in $CaCO_3$ dissolution will not affect the physics of the ocean and the biological production. Only DIC, alkalinity and saturation state will be changed. In this chapter, therefore only the changes in DIC, alkalinity and associated Ω are discussed.

5.1 Present day
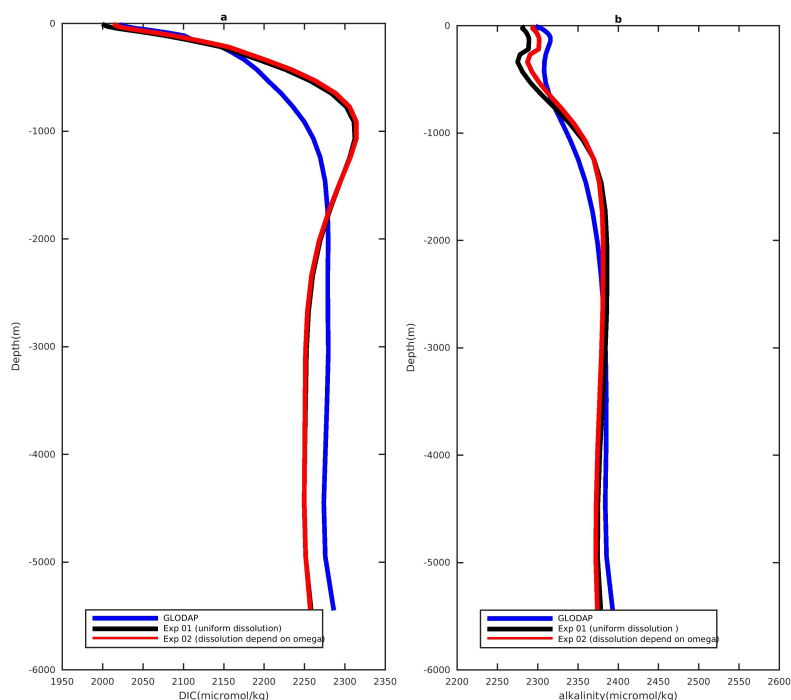
Figure 20: *Global average vertical profile of DIC and alkalinity from observational and model data (with and without Ω dependent dissolution); DIC profile denoted by (a) whereas (b) denotes the alkalinity.*

Figure 20 shows different global average vertical profiles for DIC (figure 20.a) and alkalinity (figure 20.b) obtained from the GLODAP and present day model simulations with (EXP 02) and without (EXP 01) Ω dependent dissolution. In case of DIC and alkalinity, the difference in between observational data and model simulation (EXP 01) has been observed at mid depth has been discussed briefly in chapter 3.1 (figure 7 and 8).

Comparing EXP 02 to EXP 01 there are some differences in DIC and alkalinity which are stronger near the surface ocean. Alkalinity from EXP 02 is on average higher by approximately 5.22 micromol/kg than the alkalinity from EXP 01 and the surface value is higher by around 12.55 micromol/kg. The differences increases from the surface to 800 m depth and then start to decrease after-that. This pattern is same for DIC. DIC from EXP 02 is higher on average by approximately 4.9 micromol/kg than the values from EXP 01 and the surface value is higher by around 13.65 micromol/kg.
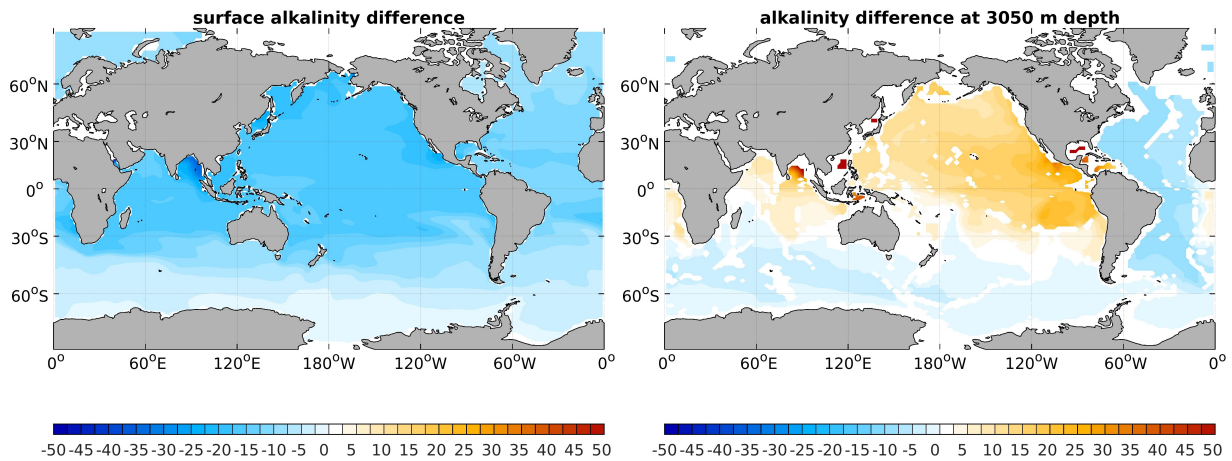
Figure 21: *Distribution of alkalinity difference from model data (uniform dissolution - Ω dependent dissolution) at the surface and 3050 m depth.*

The horizontal distribution of alkalinity difference between uniform and Ω dependent dissolution model run is shown in figure 21 at the surface and 3050 m depth. From the figure 21, it is clear that the surface alkalinity from EXP 02 is higher all over the world ocean than the alkalinity from EXP 01. The equatorial Pacific and Indian Ocean shows little increasing pattern than the Atlantic and Southern Ocean. At the depth of 3050 m, the difference pattern is not similar all over the ocean. The alkalinity concentration from Ω dependent dissolution model run is higher in the Atlantic and Southern Ocean while the equatorial Pacific and Indian Ocean show the lower alkalinity concentration.

As alkalinity and DIC change with the changes of dissolution rate, ocean saturation state (Ω) also changes. Figure 22 shows the global distribution of saturation state (Ω) of calcite from the two different dissolution dependency model run at the surface and at 3050 m depth and also their differences. The saturation state of $CaCO_3$ is higher at the surface than in the deep ocean. The surface distribution of Omega from two different model run shows qualitatively similar
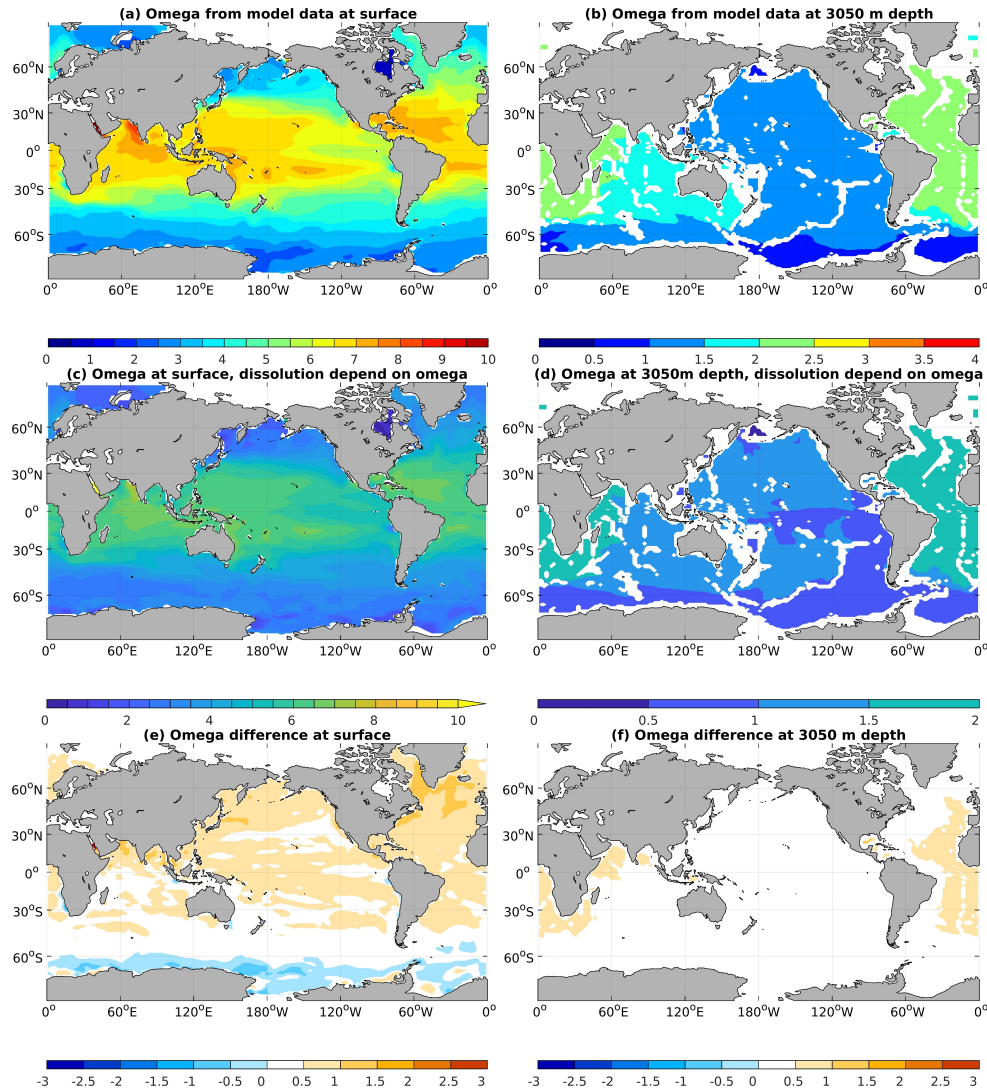
Figure 22: *Global distribution of saturation state (Ω) of calcite from model data (uniform and Ω dependent dissolution and also their differences at the surface and at 3050 m depth;(a and b) represent the value from unform dissolution whereas (c and d) denotes Ω from Ω dependent dissolution model run, (a and c) for the surface and (b and d) at 3050 m depth, surface difference shown by (e) where (f) represent difference at 3050 m depth .*

patterns, high in the subtropical regions and lower towards the high latitude. These pattern are almost uniform all over the world ocean. From the surface omega difference plot (uniform dissolution – Ω dependent dissolution) it is obvious to say that Ω from uniform dissolution is

higher all over the world ocean except the Southern Ocean. Surface Ω value from the uniform model simulation shows a higher value in the red sea, a slightly higher value in northern high latitude of Atlantic Ocean in comparison to model simulation from Ω dependent dissolution.

At 3050 m depth, omega value from EXP 01 and EXP 02 also shows the similar pattern with slightly higher Ω values at the Atlantic Ocean than the Pacific Ocean. The reason for this is that the carbonate ion concentration decreases from the Atlantic towards the Pacific as DIC increases. The difference between alkalinity and DIC is larger in the Atlantic than the Pacific because along with the conveyor belt the alkalinity increases not as much DIC. In the deeper ocean, the omega from uniform dissolution shows slightly higher values than the Ω dependent dissolution in the Atlantic Ocean approximately in between $45°$ S $– 45°$ N and some subtropics part in the Indian Ocean where the Pacific Ocean shows quite similar pattern. Figure
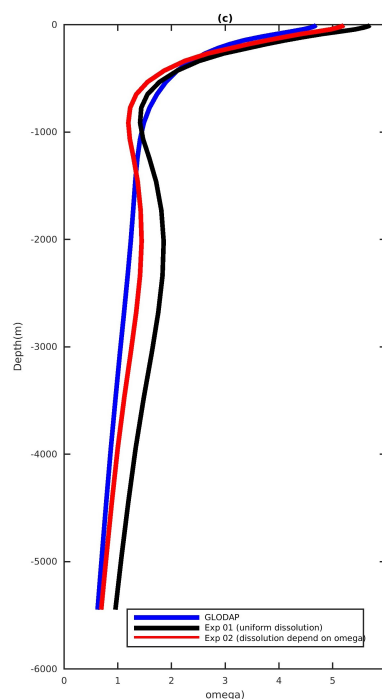
Figure 23: *Global average vertical profile of saturation state (Ω) of calcite (dimensionless) from observational and model data(with and without Ω dependent dissolution).*

23 shows the global average vertical profiles for Ω obtained from the observational data and from the simulations with and without dissolution dependency on omega. Both model profiles shows a decreasing pattern with depth with an intermediate minimum at around 800 m depth, while the data based profile shows only the decrease. This is probably due to the too strong remineralization at that depth also evident in the DIC profile (figure 20.a). The global average vertical profile of omega from model simulation EXP 02 is much closer to the observational data than the Ω from EXP 01 showing that this parameterization improves the model results.

5.2 LGM

6 Summary and discussion

This research deal with the changes in $CaCO_3$ dissolution in the LGM and present ocean. $CaCO_3$ dissolution changes is related with the degree of ocean saturation state that is further linked to the oceanic distribution of alkalinity, DIC, salinity temperature etc. To analyse the changes four different model simulation has been done: two for the present day and another two for the LGM. At first one baseline model simulation for the present day has been done with uniform dissolution and results have been compared to the observational data (GLODAP.v2). Global distribution of surface and deep ocean alkalinity and DIC from the baseline simulation show quite similar pattern to the observational data with low value at the surface and high in the deeper ocean. Compared to model data, the surface observational alkalinity in the South Atlantic and in the South Pacific seems to be slightly higher in the subtropics. There is a difference in that the highest values in alkalinity in the deep ocean are found in the Indian Ocean in the model, while the maximum is distributed more broadly in the Indian and the Pacific Ocean for the observational data. This feature can be related to figure 18 where the model has relatively high $CaCO_3$ export production in the Indian Ocean. Average vertical profile of alkalinity and DIC compared to GLODAP.v2. (figure 7 and 8) shows that the too much remineralization in the water column and too high $CaCO_3$ dissolution is happening at the intermediate depth.

Then LGM model simulation has been done with atmospheric forcing taken from coupled ocean-atmosphere simulations performed with COSMOS [Zhang et al., 2013] to investigate the physical and biogeochemical changes between LGM and present day.

The model simulation under the glacial boundary conditions simulates a deep salty and less temperate ocean than the present day. The main changes in oceanic circulation are associated with a shoaling and a weakening of the Atlantic meridional overturning cell and increase of Antarctic Bottom Water formation with a much stronger penetration of AABW into the Atlantic Ocean. In the present day AABW is present only in the southern Atlantic (figure 10.b), while glacial AABW fills the entire Atlantic basin below 2000 m (Figure 10.a). The resulted shoaling and weakening Atlantic meridional overturning is consisted with many other model simulations result [Buchanan et al., 2016b, Völker and Köhler, 2013, Zhang et al., 2013, Brovkin et al., 2007].

The change in simulated sea surface temperature (SST) between LGM and present day shows the greatest cooling in the equatorial region, high latitude and least cooling in the subtropics. The mean LGM SST was 2.7° C cooler than the present day. This changes falls within

the range of estimates ($\sim$ 2-4° C) produced by other climate models [Alder and Hostetler, 2015, Annan and Hargreaves, 2013, Braconnot et al., 2007]. The average Atlantic LGM ocean temperature is cooler by 3.8° C and the Pacific LGM is cooler by 2.1° C than the present day.

The overall LGM salinity is higher than the present day because of lowering of sea level by 116 m. Expansion of large sea ice give advantages to the increase of sea ice transport out from the AABW formation area, which increases the salinity of AABW and decreases surface salinity in the Atlantic Ocean. The simulated increase of AABW salinity is consistent with [Adkins et al., 2002].

Two new model simulations (EXP 02 and EXP 04) with a modified dissolution rate (Ω dependent dissolution) for the LGM and present day have been done to to see how alkalinity, DIC and saturation horizon vary from the previous model runs with uniform dissolution. Compared to global observation (GLODAP.v2), Present day Ω dependent dissolution model simulation provides a better DIC and alkalinity profile than the uniform dissolution present day simulation (EXP 01) with a discrepancy at the mid depth. The difference in alkalinity from global observation to Ω dependent dissolution is around 4.8 micromol/kg where this difference is higher by $\sim$ 10.1 micromol/kg from global observation to uniform dissolution.

Associated with the change in DIC and alkalinity, ocean saturation state also changes. The Ω from both model run shows qualitatively similar pattern with the observational data: decreasing along with depth with an intermediate minimum at around 800 m depth, while the data based profile shows only the decrease. The global average vertical profile of omega from Ω dependent model simulation is much closer to the observational data (with difference is only around 0.13) than the Ω from uniform dissolution model run (difference is around 0.48) showing that this parameterization improves the model results.

7 Conclusion

Oceanic calcium carbonate production in surface waters and dissolution and accumulation in sediments has a direct effect on the dissolved inorganic carbon and alkalinity as well as influences the oceanic uptake capacity of atmospheric CO_2 by determining the surface water CO_2 concentration. In this study, modeled saturation state as well as DIC and alkalinity are compared with the observational data. The saturation horizon is directly related to the oceanic content of DIC and alkalinity. Comparing the model simulation with the observation, the general pattern for DIC, alkalinity and for omega values are quite similar. But there is some disagreement in that the difference between the deep North Atlantic and Pacific is too low. That seems to be caused by a somewhat too shallow remineralization of POC and too much dissolution of $CaCO_3$ in the upper water column.

Comparing to the present day model, model simulation under the glacial boundary conditions simulates a deep salty and less temperate ocean than the present day. The main changes in oceanic circulation are associated with a shoaling and a weakening of the Atlantic meridional overturning cell and increase of Antarctic Bottom Water formation with a much stronger penetration of AABW into the Atlantic Ocean. Distribution of alkalinity, DIC and associated saturation horizon of the ocean are aslo changed with the change of atmospheric forching from present to glacial climate. The overall LGM salinity and nutrient concentration is higher than the present day because of lowering of sea level by 116 m. LGM alkalinity concentration is lower at the depth range in between $\sim$ 0 - 2000 m but higher at the deeper ocean than the present day. The surface alkalinity changes driven by the salinity changes along with the location changes of different water mass between LGM and present day. Increases of salinity normalised alkalinity below 2000 m in the ocean point to changes in the vertical flux of POC and $CaCO_3$ as further factors.

In this study it is tested whether an improvement in the modeled alkalinity, DIC and saturation state (Ω) distribution can be reached by making the dissolution depend on the $CaCO_3$ saturation state. It is shown that the making calcite dissolution depend on the $CaCO_3$ saturation state gives much more improved distribution of alkalinity, DIC and saturation state (Ω) that is much closer to the observational data.

References

A. Adcroft, C. Hill, J.-M. Campin, J. Marshall, and P. Heimbach. Overview of the formulation and numerics of the MIT GCM. In *Proceedings of the ECMWF seminar series on Numerical Methods, Recent developments in numerical methods for atmosphere and ocean modelling*, pages 139–149, 2004.

J. F. Adkins, K. McIntyre, and D. P. Schrag. The salinity, temperature, and $\delta^{18}O$ of the glacial deep ocean. *Science*, 298(5599):1769–1773, 2002. ISSN 0036-8075. doi: 10.1126/science.1076252.

J. R. Alder and S. W. Hostetler. Global climate simulations at 3000-year intervals for the last 21 000 years with the genmom coupled atmosphere–ocean model. *Climate of the Past*, 11 (3):449–471, 2015. doi: 10.5194/cp-11-449-2015.

J. D. Annan and J. C. Hargreaves. A new global reconstruction of temperature changes at the last glacial maximum. *Climate of the Past*, 9(1):367–376, 2013. doi: 10.5194/cp-9-367-2013.

J. Antonov, D. Seidov, T. Boyer, R. Locarnini, A. Mishonov, H. Garcia, O. Baranova, M. Zweng, and D. Johnson. World Ocean Atlas 2009, Volume 2: Salinity, edited by: Levitus, S. *NOAA Atlas NESDIS*, 69, 2010.

D. Archer. Equatorial Pacific calcite preservation cycles: Production or dissolution? *Paleoceanography*, 6(5):561–571, 1991. doi: 10.1029/91PA01630.

R. S. Arvidson, I. E. Ertan, J. E. Amonette, and A. Luttge. Variation in calcite dissolution rates: A fundamental problem? *Geochimica et Cosmochimica Acta*, 67(9):1623 – 1634, 2003. doi: 10.1016/S0016-7037(02)01177-8.

O. Aumont, J. C. Orr, P. Monfray, G. Madec, and E. Maier-Reimer. Nutrient trapping in the equatorial pacific: The ocean circulation solution. *Global Biogeochemical Cycles*, 13(2): 351–369, 1999. doi: 10.1029/1998GB900012.

O. Aumont, E. Maier-Reimer, S. Blain, and P. Monfray. An ecosystem model of the global ocean including Fe, Si, P colimitations. *Global Biogeochemical Cycles*, 17(2), 2003. doi: 10.1029/2001GB001745.

W. Balch, D. Drapeau, B. Bowler, and E. Booth. Prediction of pelagic calcification rates using satellite measurements. *Deep Sea Research Part II: Topical Studies in Oceanography*, 54(5): 478–495, 2007.

W. M. Balch, H. R. Gordon, B. C. Bowler, D. T. Drapeau, and E. S. Booth. Calcium carbonate measurements in the surface global ocean based on Moderate-Resolution Imaging Spectroradiometer data. *Journal of Geophysical Research: Oceans*, 110(C7), 2005. doi: 10.1029/2004JC002560.

G. Battaglia, M. Steinacher, and F. Joos. A probabilistic assessment of calcium carbonate export and dissolution in the modern ocean. *Biogeosciences*, 13(9):2823–2848, 2016. doi: 10.5194/bg-13-2823-2016.

V. Benz, O. Esper, R. Gersonde, F. Lamy, and R. Tiedemann. Last glacial maximum sea surface temperature and sea-ice extent in the pacific sector of the southern ocean. *Quaternary Science Reviews*, 146:216 – 237, 2016. ISSN 0277-3791. doi: https://doi.org/10.1016/j.quascirev.2016.06.006.

W. M. Berelson, W. M. Balch, R. Najjar, R. A. Feely, C. Sabine, and K. Lee. Relating estimates of $CaCO_3$ production, export, and dissolution in the water column to measurements of $CaCO_3$ rain into sediment traps and dissolution on the sea floor: A revised global carbonate budget. *Global Biogeochemical Cycles*, 21(1):GB1024, 2007. doi: 10.1029/2006GB002803.

B. P. Boudreau and D. E. Canfield. A comparison of closed-and open-system models for pore-water pH and calcite-saturation state. *Geochimica et Cosmochimica Acta*, 57(2):317–334, 1993.

E. A. Boyle. Cadmium and delta13c paleochemical ocean distributions during the stage 2 glacial maximum. *Annual Review of Earth and Planetary Sciences*, 20(1):245–287, 1992. doi: 10.1146/annurev.ea.20.050192.001333.

P. Braconnot, B. Otto-Bliesner, S. Harrison, S. Joussaume, J.-Y. Peterchmitt, A. Abe-Ouchi, M. Crucifix, E. Driesschaert, T. Fichefet, C. D. Hewitt, M. Kageyama, A. Kitoh, A. Laîné, M.-F. Loutre, O. Marti, U. Merkel, G. Ramstein, P. Valdes, S. L. Weber, Y. Yu, and Y. Zhao. Results of pmip2 coupled simulations of the mid-holocene and last glacial maximum ndash; part 1: experiments and large-scale features. *Climate of the Past*, 3(2):261–277, 2007. doi: 10.5194/cp-3-261-2007.

W. Broecker and T. Peng. Tracers in the sea, 690 pp. *Lamont-Doherty Geological Observatory, Palisades, NY*, 1982.

V. Brovkin, A. Ganopolski, D. Archer, and S. Rahmstorf. Lowering of glacial atmospheric co2

in response to changes in oceanic circulation and marine biogeochemistry. *Paleoceanography*, 22(4), 2007. ISSN 1944-9186. doi: 10.1029/2006PA001380.

C. W. Brown and J. A. Yoder. Coccolithophorid blooms in the global ocean. *Journal of Geophysical Research: Oceans*, 99(C4):7467–7482, 1994. doi: 10.1029/93JC02156.

P. J. Buchanan, R. J. Matear, A. Lenton, S. J. Phipps, Z. Chase, and D. M. Etheridge. The simulated climate of the last glacial maximum and insights into the global marine carbon cycle. *Climate of the Past*, 12(12):2271–2295, 2016a. doi: 10.5194/cp-12-2271-2016.

P. J. Buchanan, R. J. Matear, A. Lenton, S. J. Phipps, Z. Chase, and D. M. Etheridge. The simulated climate of the last glacial maximum and insights into the global marine carbon cycle. *Climate of the Past*, 12(12):2271–2295, 2016b. doi: 10.5194/cp-12-2271-2016.

C.-T. A. Chen. Rates of calcium carbonate dissolution and organic carbon decomposition in the north pacific ocean. *Journal of the Oceanographical Society of Japan*, 46(5):201–210, Oct 1990. ISSN 1573-868X. doi: 10.1007/BF02124907.

S.-N. Chung, K. Lee, R. A. Feely, C. L. Sabine, F. J. Millero, R. Wanninkhof, J. L. Bullister, R. M. Key, and T.-H. Peng. Calcium carbonate budget in the Atlantic Ocean based on water column inorganic carbon chemistry. *Global Biogeochemical Cycles*, 17(4), 2003. doi: 10.1029/2002GB002001. 1093.

W. Curry and G. Lohmann. Carbon isotopic changes in benthic foraminifera from the western south atlantic: Reconstruction of glacial abyssal circulation patterns. *Quaternary Research*, 18(2):218 – 235, 1982. ISSN 0033-5894. doi: https://doi.org/10.1016/0033-5894(82)90071-0.

T. L. Delworth, P. U. Clark, M. Holland, T. Johns, T. Kuhlbrodt, C. Lynch-Stieglitz, R. Seager, A. J. Weaver, and R. Zhang. The potential for abrupt change in the atlantic meridional overturning circulation. In *Abrupt Climate Change. A report by the U.S. Climate Change Science Program and the Subcommittee on Global Change Research.*, pages 258–359. U. S. Geological Survey, Reston, VA, December 2008.

DOE. : Handbook of methods for the analysis of the various parameters of the carbon dioxide system in sea water,ag and goyet, c.(eds.) version 2. *ORNL/CDIAC-74*, 20, 1994.

J. C. Duplessy, N. J. Shackleton, R. G. Fairbanks, L. Labeyrie, D. Oppo, and N. Kallel. Deepwater source variations during the last climatic cycle and their impact on the global

deepwater circulation. *Paleoceanography*, 3(3):343–360, 1988. ISSN 1944-9186. doi: 10.1029/PA003i003p00343.

S. Emerson and M. Bender. Carbon fluxes at the sediment-water interface of the deep-sea: calcium carbonate preservation. *Journal of Marine Research*, 39:139–162, 1981.

H. Garcia, R. Locarnini, T. Boyer, J. Antonov, and S. Levitus. World Ocean Database 2005, Volume 4: Nutrients (phosphate, nitrate, silicate). *NOAA Atlas NESDIS*, (4), 2006.

H. Garcia, R. Locarnini, T. Boyer, and J. Antonov. World Ocean Atlas 2009, vol. 4, Nutrients (Phosphate, Nitrate, Silicate), NOAA Atlas NESDIS, vol. 71. *US Gov. Print. Off., Washington, DC*, 2010.

M. Gehlen, R. Gangstø, B. Schneider, L. Bopp, O. Aumont, and C. Ethe. The fate of pelagic $CaCO_3$ production in a high CO_2 ocean: a model study. *Biogeosciences*, 4(4):505–519, 2007. doi: 10.5194/bg-4-505-2007.

R. J. Geider, H. L. MacIntyre, and T. M. Kana. A dynamic regulatory model of phytoplanktonic acclimation to light, nutrients, and temperature. *Limnology and Oceanography*, 43(4):679–694, 1998. doi: 10.4319/lo.1998.43.4.0679.

R. Gersonde, X. Crosta, A. Abelmann, and L. Armand. Sea-surface temperature and sea ice distribution of the southern ocean at the {EPILOG} last glacial maximum—a circum-antarctic view based on siliceous microfossil records. *Quaternary Science Reviews*, 24(7–9):869 – 896, 2005. ISSN 0277-3791. doi: 10.1016/j.quascirev.2004.07.015. Multiproxy Approach for the Reconstruction of the Glacial Ocean surface.

B. Hales. Respiration, dissolution, and the lysocline. *Paleoceanography*, 18(4), 2003. doi: 10.1029/2003PA000915.

B. Hales and S. Emerson. Calcite dissolution in sediments of the Ceara Rise: In situ measurements of porewater O_2, pH, and CO_2 (aq). *Geochimica et Cosmochimica Acta*, 61(3): 501–514, 1997a.

B. Hales and S. Emerson. Evidence in support of first-order dissolution kinetics of calcite in seawater. *Earth and Planetary Science Letters*, 148(1-2):317–327, 1997b.

J. Hauck, C. Völker, T. Wang, M. Hoppema, M. Losch, and D. A. Wolf-Gladrow. Seasonally different carbon flux changes in the Southern Ocean in response to the southern annular mode. *Global Biogeochemical Cycles*, 27(4):1236–1245, 2013. doi: 10.1002/2013GB004600.

H. Jansen. Modelling the marine carbonate pump and its implications on the atmospheric CO_2 concentration. *Bremen: Universität Bremen (Dissertation)*, pages 1–128, 2001.

H. Jansen, R. Zeebe, and D. Wolf-Gladrow. Modelling the dissolution of settling $CaCO_3$ in the ocean. *Global Biogeochemical Cycles, 16 (2)*, 11:1–16, 2002. doi: 10.1029/2000GB001279.

X. Jin, R. G. Najjar, F. Louanchi, and S. C. Doney. A modeling study of the seasonal oxygen budget of the global ocean. *Journal of Geophysical Research: Oceans*, 112(C5):C05017, 2007. doi: 10.1029/2006JC003731.

R. S. Keir. The dissolution kinetics of biogenic calcium carbonates in seawater. *Geochimica et Cosmochimica Acta*, 44(2):241–252, 1980.

R. M. Key, A. Kozyr, C. L. Sabine, K. Lee, R. Wanninkhof, J. L. Bullister, R. A. Feely, F. J. Millero, C. Mordy, and T.-H. Peng. A global ocean carbon climatology: Results from Global Data Analysis Project (GLODAP). *Global Biogeochemical Cycles*, 18(4), 2004.

I. Kriest and A. Oschlies. On the treatment of particulate organic matter sinking in large-scale models of marine biogeochemical cycles. *Biogeosciences*, 5(1):55–72, 2008. doi: 10.5194/bg-5-55-2008.

W. G. Large and S. G. Yeager. *Diurnal to decadal global forcing for ocean and sea-ice models: the data sets and flux climatologies*. NCAR technical notes. National Center for Atmospheric Research Boulder, 2004. doi: 10.5065/D6KK98Q6.

S. K. Lauvset, R. M. Key, A. Olsen, S. van Heuven, A. Velo, X. Lin, C. Schirnick, A. Kozyr, T. Tanhua, M. Hoppema, S. Jutterström, R. Steinfeldt, E. Jeansson, M. Ishii, F. F. Perez, T. Suzuki, and S. Watelet. A new global interior ocean mapped climatology: the $1° × 1°$ GLODAP version 2. *Earth System Science Data*, 8(2):325–340, 2016. doi: 10.5194/essd-8-325-2016.

D. W. Lea. Constraints on the alkalinity and circulation of glacial circumpolar deep water from benthic foraminiferal barium. *Global Biogeochemical Cycles*, 7(3):695–710, 1993. ISSN 1944-9224. doi: 10.1029/93GB01536.

R. Locarnini, A. Mishonov, J. Antonov, T. Boyer, H. Garcia, O. Baranova, M. Zweng, and D. Johnson. World Ocean Atlas 2009, vol. 1. *Temperature, NOAA Atlas NESDIS*, 68, 2010.

J. Marshall, A. Adcroft, C. Hill, L. Perelman, and C. Heisey. A finite-volume, incompressible navier stokes model for studies of the ocean on parallel computers. *Journal of Geophysical Research: Oceans*, 102(C3):5753–5766, 1997. doi: 10.1029/96JC02775.

F. J. Millero. Thermodynamics of the carbon dioxide system in the oceans. *Geochimica et Cosmochimica Acta*, 59(4):661–677, 1995. doi: 10.1016/0016-7037(94)00354-O.

F. J. Millero, K. Lee, and M. Roche. Distribution of alkalinity in the surface waters of the major oceans. *Marine Chemistry*, 60(1):111 – 130, 1998. ISSN 0304-4203. doi: https://doi.org/10.1016/S0304-4203(97)00084-4.

J. Milliman and A. Droxler. Neritic and pelagic carbonate sedimentation in the marine environment: ignorance is not bliss. *Geologische Rundschau*, 85(3):496–504, 1996. doi: 10.1007/BF02369004.

J. Milliman, P. Troy, W. Balch, A. Adams, Y.-H. Li, and F. Mackenzie. Biologically mediated dissolution of calcium carbonate above the chemical lysocline? *Deep Sea Research Part I: Oceanographic Research Papers*, 46(10):1653–1669, 1999. doi: 10.1016/S0967-0637(99)00034-5.

J. W. Morse. Dissolution kinetics of calcium carbonate in sea water; V, effects of natural inhibitors and the position of the chemical lysocline. *American Journal of Science*, 274(6): 638–647, 1974. doi: 10.2475/ajs.274.6.638.

J. W. Morse and R. A. Berner. Dissolution kinetics of calcium carbonate in sea water; I, A kinetic origin for the lysocline. *American Journal of Science*, 272(9):840–851, 1972. doi: 10.2475/ajs.272.9.840.

A. Mucci. The solubility of calcite and aragonite in seawater at various salinities, temperatures, and one atmosphere total pressure. *American Journal of Science*, 283(7):780–799, 1983. doi: 10.2475/ajs.283.7.780.

J. C. Orr and J.-M. Epitalon. Improved routines to model the ocean carbonate system: mocsy 2.0. *Geoscientific Model Development*, 8(3):485–499, 2015. doi: 10.5194/gmd-8-485-2015.

R. K. Pachauri and A. Reisinger, editors. *Climate Change 2007: Synthesis Report. Contribution of Working Groups I, II and III to the Fourth Assessment Report of the Intergovernmental Panel on Climate Change.* IPCC, Geneva, Switzerland, 2007.

J. Sarmiento and N. Gruber. *Ocean Biogeochemical Dynamics*. Princeton University Press, 2006. ISBN 9780691017075.

J. Sarmiento, J. Dunne, A. Gnanadesikan, R. Key, K. Matsumoto, and R. Slater. A new estimate of the $CaCO_3$ to organic carbon export ratio. *Global Biogeochemical Cycles*, 16(4), 2002.

V. Schourup-Kristensen, D. Sidorenko, D. A. Wolf-Gladrow, and C. Völker. A skill assessment of the biogeochemical model REcoM2 coupled to the Finite Element Sea Ice–Ocean Model (FESOM 1.3). *Geoscientific Model Development*, 7(6):2769–2802, 2014. doi: 10.5194/gmd-7-2769-2014.

D. M. Sigman and E. A. Boyle. Glacial/interglacial variations in atmospheric carbon dioxide. *Nature*, 407(6806):859–869, 2000. doi: 10.1038/35038000.

L. D. Talley. Distribution and formation of north pacific intermediate water. *Journal of Physical Oceanography*, 23(3):517–537, 1993. doi: 10.1175/1520-0485(1993)023¡0517:DAFONP¿2.0.CO;2.

L. D. Talley. Closure of the global overturning circulation through the indian, pacific, and southern oceans: Schematics and transports. *Oceanography*, 26(1):80–97, 2013. doi: 10.5670/oceanog.2013.07.

R. Vhuiyan. Improving the Description of the Formation of $CaCO_3$ in a Global Biogeochemical Model. Master's thesis, University of Bremen, 2016.

C. Völker and P. Köhler. Responses of ocean circulation and carbon cycle to changes in the position of the southern hemisphere westerlies at last glacial maximum. *Paleoceanography*, 28(4):726–739, 2013. ISSN 1944-9186. doi: 10.1002/2013PA002556.

P. Westbroek, C. W. Brown, J. van Bleijswijk, C. Brownlee, G. J. Brummer, M. Conte, J. Egge, E. Fernández, R. Jordan, M. Knappertsbusch, et al. A model system approach to biological climate forcing. The example of Emiliania huxleyi. *Global and Planetary Change*, 8(1-2): 27–46, 1993.

D. A. Wolf-Gladrow, R. E. Zeebe, C. Klaas, A. Körtzinger, and A. G. Dickson. Total alkalinity: The explicit conservative expression and its application to biogeochemical processes. *Marine Chemistry*, 106(1):287–300, 2007. doi: 10.1016/j.marchem.2007.01.006.

Y. Yamanaka and E. Tajika. The role of the vertical fluxes of particulate organic matter and calcite in the oceanic carbon cycle: Studies using an ocean biogeochemical general circulation model. *Global Biogeochemical Cycles*, 10(2):361–382, 1996.

R. E. Zeebe and D. A. Wolf-Gladrow. *CO₂ in seawater: Equilibrium, Kinetics, Isotopes*, volume 65 of *Elsevier oceanography series*. Elsevier, 2001.

X. Zhang, G. Lohmann, G. Knorr, and X. Xu. Different ocean states and transient characteristics in last glacial maximum simulations and implications for deglaciation. *Climate of the Past*, 9 (5):2319–2333, 2013. doi: 10.5194/cp-9-2319-2013.

I. Zondervan, R. E. Zeebe, B. Rost, and U. Riebesell. Decreasing marine biogenic calcification: A negative feedback on rising atmospheric $p\mathrm{CO}_2$. *Global Biogeochemical Cycles*, 15(2): 507–516, 2001. doi: 10.1029/2000GB001321.